1 Hot spots, hot moments, and spatiotemporal drivers of soil

2 CO₂ flux in temperate peatlands using UAV remote sensing

- 3 Yanfei Li^{1*}, Maud Henrion¹, Angus Moore¹, Sébastien Lambot¹, Sophie
- 4 Opfergelt¹, Veerle Vanacker¹, François Jonard^{2†}, Kristof Van Oost^{1†}
- ¹ Earth and Life Institute, Université catholique de Louvain, 1348 Louvain-la-Neuve, Belgium.
- 6 ² Earth Observation and Ecosystem Modelling Laboratory, SPHERES Research Unit, Université de
- 7 Liège, 4000 Liège, Belgium.
- 8 *Correspondence to: Yanfei Li (email: yanfei.li@uclouvain.be).
- 9 † These authors are co-last authors.

Abstract

11

12

13

14

15

16

17

18

19

20

21

22

23

24

25

26

27

28

29

30

31

32

33

34

35

36

37

38

CO₂ emissions from peatlands exhibit substantial spatial and temporal spatiotemporal variability due to their heterogeneous nature, presenting challenges forto identifying their the underlying drivers and forto accurately quantifying and modeling CO₂ fluxes. Here, we integrated field measurements with Unmanned Aerial Vehicle (UAV)-based multi-sensor remote sensing to investigate soil respiration across a temperate peatland landscape. Our research addressed two key questions: (1) How do environmental factors control the spatial temporalspatiotemporal distribution of soil respiration across complex landscapes? (2) How do spatial and temporal peaks (i.e., hot spots and hot moments) of biogeochemical processes influence landscape-level CO₂ fluxes? We find that dynamic variables (i.e., soil temperature and moisture) play significant roles in shaping CO₂ flux variations, contributing 43 % to seasonal variability and 29 % to spatial variance, followed by semi-dynamic variables (i.e., Normalized Difference Vegetation Index (NDVI) and root biomass) (19 % and 24 %). Relatively static variables (i.e., soil organic carbon (SOC)-stock and CNcarbon to nitrogen ratio) have a minimal influence on seasonal variation (2 %) but contribute more to spatial variance (10 %). Additionally, predicting time series of CO₂ fluxes is feasible by using key environmental variables (test set: coefficient of determination $(R^2) = 0.74$, Root Mean Square Error (RMSE) = 0.57 μmol m⁻² s⁻¹, Kling-Gupta Efficiency (KGE) = 0.77), while UAV remote sensing is an effective tool for mapping daily soil respiration (test set: $R^2 = 0.75$, RMSE = 0.564 μ mol m⁻² s⁻¹, $\underline{KGE} = 0.83$). By the integration of in-situ high-resolution time-lapse monitoring and spatial mapping, we find that despite occurring in 10 % of the year, hot moments (i.e., periods of time which have a disproportional high (> 90th percentile) CO₂ fluxes compared to the surrounding) contribute 28 %-31 % of the annual CO₂ fluxes. Meanwhile, hot spots (i.e., locations which CO₂ fluxes higher than 90th percentile)—representing 10 % of the area—account for about 20 % of CO₂ fluxes across the landscape. Our study demonstrates that integrating UAV-based remote sensing with field surveys improves the understanding of soil respiration mechanisms across timescales in complex landscapes. This will providing provide insights into carbon dynamics and supporting peatland conservation and climate change mitigation efforts. Keywords: Peatlands, Soil respiration, Greenhouse gas (CO₂) emission, CO₂ hot spots, CO₂ hot moments, Multi-sensor UAV remote sensing, Global warming

1 Introduction

39

40 Peatlands are globally distributed ecosystems that cover an area of 6.75 million km² and store 41 approximately 600 942.09 ± 312 Gt of carbon (Widyastuti et al., 2025) (Yu et al., 2010), despite covering 42 less than 4 % of the Earth's land surface (Xu et al., 2018). However, rising concerns exist over peatlands 43 shifting from carbon sinks to carbon sources due to the impact of climate change (Dorrepaal et al., 2009; 44 Hopple et al., 2020; Huang et al., 2021), land use/cover conversion (Deshmukh et al., 2021; Leifeld et 45 al., 2019; Prananto et al., 2020), and other disturbances (Turetsky et al., 2015; Wilkinson et al., 2023). 46 In Europe, it has been reported that nearly half of the peatlands are suffering degradation, primarily due 47 to drainage for agricultural or forestry activities (Leifeld et al., 2019; UNEP, 2022). As a consequence, 48 European peatlands currently emit up to 580 Mt CO₂-eq per year across the continent (UNEP, 2022). 49 Given the critical role of the peatland ecosystem in the terrestrial carbon cycle, it is therefore important 50 to understand the mechanisms driving carbon fluxes and their responses to climate change and human 51 disturbances. 52 Soil respiration, a key ecological process that releases CO₂ from peatlands into the atmosphere, in 53 peatlands_is influenced by a combination of biotic and abiotic factors. Among abiotic controls, soil 54 temperature and moisture play a crucial role in driving microbial activity and root respiration, influencing 55 CO₂ fluxes across daily to annual scales (Evans et al., 2021; Fang and Moncrieff, 2001; Hoyt et al., 2019; 56 Juszczak et al., 2013; Swails et al., 2022). Water table fluctuations alter oxygen availability and 57 distribution within the soil profile, directly affecting microbial processes and carbon emissions (Evans et 58 al., 2021; Hoyt et al., 2019). Atmospheric pressure affects the transport of gases between the soil surface 59 and the atmosphere, thereby modulating the CO₂ fluxes (Lai et al., 2012; Ryan and Law, 2005). 60 Vegetation, as a key biotic factor, influences the spatiotemporal variations of soil respiration through 61 phenology, structure, and community (Acosta et al., 2017; Wang et al., 2021). In addition, soil organic 62 matter provides essential substrates for microbial activity, with previous studies suggesting that the 63 quality of organic material, rather than its quantity, primarily regulates CO2 fluxes in peatlands (Hoyos-64 Santillan et al., 2016; Leifeld et al., 2012). 65 , such as soil temperature and moisture (Evans et al., 2021; Fang and Moncrieff, 2001; Hoyt et al., 2019; 66 Juszczak et al., 2013; Swails et al., 2022; Treat et al., 2014), vegetation and root biomass (Acosta et al., 2017; Wang et al., 2021), and soil organic matter quality (Hoyos Santillan et al., 2016; Leifeld et al., 2012).

67

68

69

70

71

72

73

74

75

76

77

78

79

80

81

82

83

84

85

86

87

88

89

90

91

92

93

94

CO₂ emissions from peatlands are highly variable over space and time, presenting challenges to accurately quantify and model carbon fluxes. This may partially because peatlands are characterized by a unique microtopography, including features such as soil bencheshummocks and depressions hollows (Moore et al., 2019). These small-scale variations create differences in hydrology, temperature, biogeochemistry, and vegetation (Harris and Baird, 2019), leading to substantial spatial differences in the factors that control CO₂ fluxes and the formation of "hot spots" with elevated CO₂ emissions (Becker et al., 2008; Frei et al., 2012; Kelly et al., 2021; Kim and Verma, 1992; McClain et al., 2003). For instance, the peat surface temperature differences within a 10 m x 10 m plot characterized by hummock and hollow features can be 20°C (Rhoswen et al., 2018). In addition, peatlands experience exhibit a high sensitivity to meteorological variability highly variable weather conditions, which can trigger periods of disproportionately high CO₂ fluxes—often referred to as "hot moments"—in response to transient environmental changes, such as sudden shifts in temperature, atmospheric pressure, rainfall events, or fluctuations in the water table (Anthony and Silver, 2023; Fernandez-Bou et al., 2020). High CO₂ emissions occur from discrete areas in space (hot spots) and over short periods (hot moments), and may disproportionately contribute to the overall fluxes (Anthony and Silver, 2023; Fernandez-Bou et al., 2020).- Most studies have examined the mechanisms and contributions of hot spots and hot moments of other greenhouse gases (N₂O, CH₄) in agricultural and forestry ecosystems (Anthony and Silver, 2021; Fernandez-Bou et al., 2020; Kannenberg et al., 2020; Krichels and Yang, 2019; Leon et al., 2014), while However, research on CO₂ emission hot spots and hot moments in peatlands remains limited- (Anthony and Silver, 2021; Anthony and Silver, 2023), even though both CO2 and CH4 originate from organic matter decomposition under different redox conditions.

Identifying and quantifying hot spots and hot moments in peatlands is challenging, requiring large-scale, continuous, long-term observations. Currently, most studies on peatland soil respiration rely on point measurements taken at intervals of half a month to one month, primarily during daytime (e.g., Bubier et al. (2003); Danevčič et al. (2010); Kim and Verma (1992); Wright et al. (2013)). This spatial temporal spatiotemporal limitation hinders constrains the effective detection understanding of hot spots

and hot moments. Some studies attempted to extrapolate point data using land-use maps (McNamara et al., 2008; van Giersbergen et al., 2024; Webster et al., 2008), but uncertainties in landscape-scale fluxes increase as the number of measurement locations decreases (Arias-Navarro et al., 2017; Wangari et al., 2022; Wangari et al., 2023). While automated chamber systems improve temporal resolution and help capture hot moments (Anthony and Silver, 2023; Hoyt et al., 2019), they are typically limited to a few sampling points, and scaling up is constrained by significant resource demands. Eddy covariance towers can continuously measure net ecosystem exchange over large areas_by recording high frequency CO2 concentrations and air turbulence, providing insights into temporal variations at the ecosystem level (Abdalla et al., 2014; Rey-Sanchez et al., 2022)₃. However, the underlying controlling factors and mechanisms at the process level are difficult to infer due to the large spatial footprint. In addition, but they may not accurately representate less effective in capturing the spatial heterogeneity of peatlands (Lees et al., 2018). These limitations highlight the need for spatially robust, high-resolution methods that can characterize complementary approaches to estimate CO2 fluxes at the landscape scale with methods adapted foracross heterogeneous peatland ecosystemslandscapes.

Several studies have integrated satellite-based remote sensing datasets with on-site chamber measurements to model landscape-scale CO₂ fluxes (e.g., Azevedo et al. (2021); Junttila et al. (2021); Lees et al. (2018); Wangari et al. (2023)). Remote sensing datasets on topography and vegetation parameters serve as proxies for soil moisture, vegetation cover, and nutrient availability, enabling large-scale CO₂ emission estimates within peatlands (Lees et al., 2018). However, this approach is somewhat limited by coarse spatial (10 m to 1 km) and temporal (1 to 16 days) resolutions, which may overlook hot spots and hot moments, leading to potential over- or underestimations of CO₂ fluxes in heterogeneous (e.g., complexity in topography, diverse vegetation types, varying thermal-hydrological conditions) peatlands (Kelly et al., 2021; Simpson, 2023). This shortcoming might be overcome by using unmanned aerial vehicles (UAVs) equipped with different kinds of sensors such as Red-Green-Blue (RGB), multispectral, thermal infrared, and Light Detection and Ranging (LiDAR). UAVs offer flexible deployment and capture high-resolution spatiotemporal data (1 cm to 1 m, minutes to months) (Minasny et al., 2019) which makes them particularly suitable for monitoring complex peatland dynamics and detecting hot spots and hot moments. Thus far, UAVs have proven to be reliable tools for peatland applications, including vegetation mapping (Steenvoorden et al., 2023), topographic reconstruction

(Harris and Baird, 2019), peat depth and carbon storage estimation (Li et al., 2024), ground-water and surface water interactions (Moore et al., 2024), and moisture monitoring (Henrion et al., 2025). In a recent study, Kelly et al. (2021) utilized UAV-derived land surface temperature to estimate ecosystem respiration of a hemi-boreal fen in southern Sweden, and some studies (e.g., Pajula and Purre (2021); and Walcker et al. (2025)) employed UAV-based multispectral vegetation indices to map ecosystem CO₂ flux at high resolution. These recent studies demonstrated the great potential of UAVs for linking CO2 fluxes with environmental factors at a very high resolution, although they mainly focused on data from a single sensor. Few studies have explored the fusion of UAV-derived data from multiple sensors for mapping soil respiration across peatland landscapes. In this study, we integrate multi-sensor UAV-based remote sensing with traditional field surveys to investigate soil respiration across a temperate peatland bog landscape, located in the Belgian Hautes Fagnes. As one of the largest and most ancient peatlands in Western Europe, the Belgian Hautes Fagnes, which represents an important ecosystem for studying peatland carbon fluxes due to its sensitivity to climate change and hydrological dynamics. Our research addresses two key questions: (1) What controls the nature and strength of the relationship between soil respiration and environmental factors—such as thermal-hydrological conditions, vegetation, carbon stock and quality—across complex peatland landscapes and across spatial temporal spatiotemporal scales? To address this, we first identify the factors driving seasonal and spatial variations in soil respiration and then assess the potential for linking environmental factors to CO₂ flux at high spatiotemporal resolutions. (2) How do spatial and temporal peaks (i.e., hot spots ander hot moments) of biogeochemical processes influence landscape-level carbon fluxes? More specifically, our study has three main objectives. First, we aim to identify the factors driving seasonal and spatial variations in soil respiration. Second, we assess the potential for linking environmental factors to CO₂ flux at high spatial and temporal resolutions. ThirdFor this purpose, we discuss analyze the timing and locations and timing of hot spots and hot moments, and assessing their contributions to overall CO₂ flux budgets.

124

125

126

127

128

129

130

131

132

133

134

135

136

137

138

139

140

141

142

143

144

145

146

147

2 Materials and methods

2.1 Study site

149

150

151

152

153

154

155

156

157

158

159

160

161

162

163

164

165

166

167

168

169

170

171

172

173

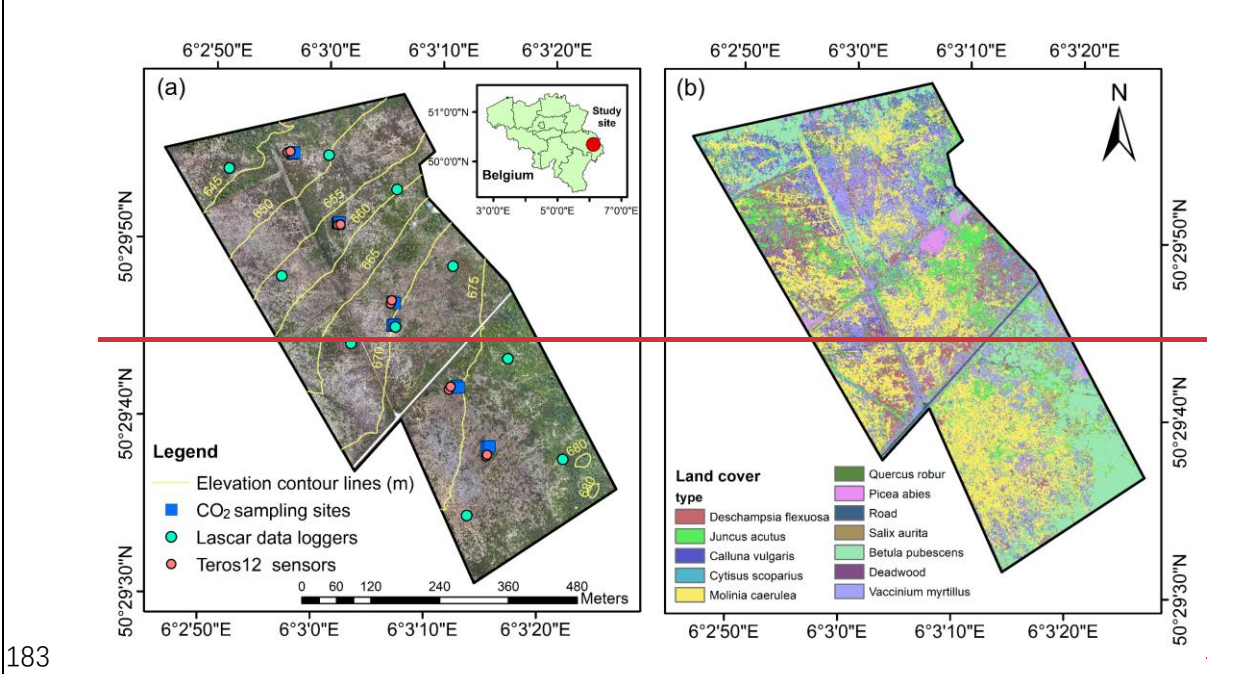
174

175

176

177

The Belgian Hautes Fagnes plateau, part of the Stavelot-Venn Massif, is located in eastern Belgium (Figure 1a). This elevated landscape experiences a humid climate, with mean annual air temperature and precipitation being approximately 6.7 °C and 1439.4 mm (period: 1971-2000), respectively (Mormal and Tricot, 2004). The peatlands in this region cover an area of 37.50 km², which primarily consist of raised bogs formed since the Late Pleistocene and grown under both oceanic and continental influences (Frankard et al., 1998; Goemaere et al., 2016). Our study site (50.49 N, 6.05 E; ~0.30 km²) is located in the upper valley of the Hoëgne River peatland bog region (Figure 1a). This ombrotrophic bog is mainly fed by precipitation and covers an area of approximately 32 hectares. The landscape exhibits complex structures, characterized by distinct SE-NW oriented topographic units (i.e., summit, topslope, shoulder, backslope, and footslope), along with diverse microtopographic features, spatiotemporal varying thermal-hydrological conditions, differences in peat thickness and carbon storage, and a range of vegetation types The site is characterized by a distinct SE NW oriented topographic gradient, with a clear transition from a low relief plateau to steep hillslopes and then to the floodplain of a broad river valley (Henrion et al., 2024; Li et al., 2024; Sougnez and Vanacker, 2011). More specifically, the summit is a low-relief, southeast-facing plateau at 675 - 680 m elevation, which transitions downslope into the topslope and concave shoulder slope positions (Figure 1a). The northwest-facing backslope is relatively steeper (average slope grade: 4.98°; elevation range: 645 - 670 m) compared to these upper units, while the footslope lies in the northwestern hillslope adjacent to Hoëgne River. The peat thickness varies spatially from 0.20 to 2.10 m across the landscape, with deeper deposits in the footslope and shallower peat at the topslope (Henrion et al., 2024; Li et al., 2024). The estimated soil organic carbon (SOC) stocks (i.e., top 1 m layer) range from 176.13 t ha⁻¹ to 856.57 t ha⁻¹, with significantly higher storage at the summit, shoulder, and footslope (Li et al., 2024). Due to the pronounced topographic gradients and microtopography, the landscape exhibits great spatiotemporal variability in rootzone soil volumetric water content (range: 0.1 – 1 cm³ cm⁻³) and water table dynamics (range: -80 – 5 cm) (Henrion et al., 2025). The area-study site was drained and planted with spruces in 1914 and 1918, while-the plantations were progressively cleared between 2000 and 2016. Seince 2017, the site has been under restoration and now primarily covered by Vaccinium myrtillus, Molinia caerulea, Juncus acutus, and native hardwood species (e.g., *Betula pubescens* and *Quercus robur*), as shown in Figure 1b. has been restored through reforestation with native hardwood species such as *Betula pubescens* and *Quercus robur*. Figure 1b shows main vegetation types across this landscape. An observation station of the Royal Meteorological Institute of Belgium (Mont Rigi, 50.51 N, 6.07 E) situated 3.07 km from northeast of the study site, records rainfall and atmospheric pressure data every 10 minutes.



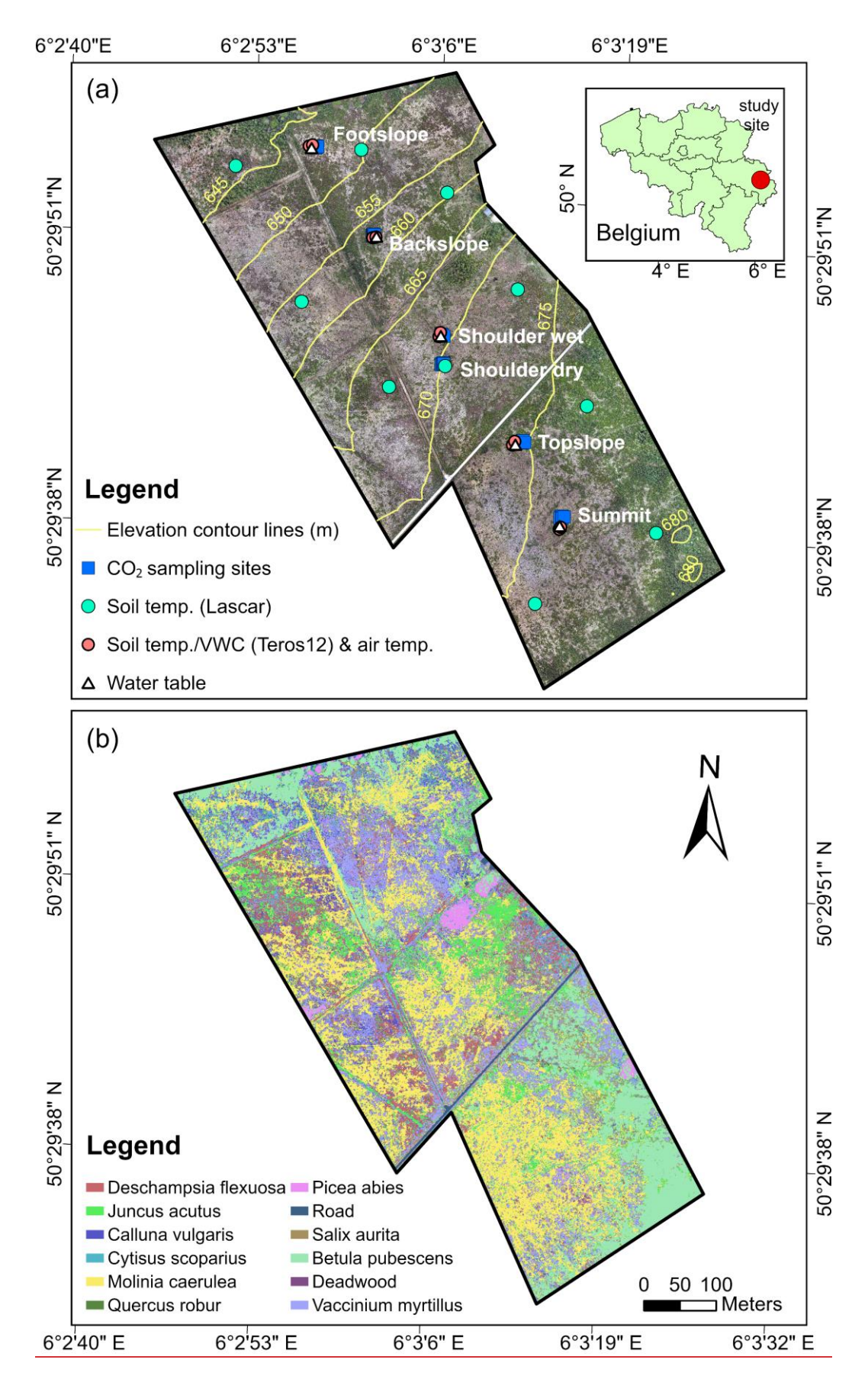


Figure 1. Maps showing the field-sampling locations (a) and land cover types (b) in the study area. Details on the land cover map are provided in our previous work (Li et al., 2024).

2.2 CO₂ flux measurement campaigns

187

188

189

190

191

192

193

194

195

196

197

198

199

200

201

202

203

204

205

206

207

208

209

210

211

212

213

214

Soil surface CO₂ flux measurements were conducted at five slope positions along the middle part of the site (Figure 1a). A portable infrared gas analyzer with an automated closed dynamic chamber (LI-8100A system, LI-COR, United States; accuracy: ± 1.5 %) was used to monitor CO₂ fluxes at 33 sites biweekly from December 2022 to March 2024 (Figure S1). The dominant vegetation type of each slope position was recorded. At each slope position Next, six collars (20 cm diameter) were installed randomly at each position, spaced 1-5 meters apart, to capture small-scale spatial variability. Given the high variability in soil water content at the shoulder position (Henrion et al., 2025). While at the shoulder, considering the heterogeneous soil water conditions, six collars were installed in drier areas (i.e., Shoulder dry) and another three in wetter areas (i.e., Shoulder wet). All vegetation within the collars was removed. During each campaign, monitoring was conducted between 9:00 and 16:00. At each site, the CO₂ flux (µmol m ² s⁻¹) in the chamber was measured for 2.5 minutes per observation. Simultaneously, soil surface temperature (0-10 cm) and volumetric water content (VWC) during each CO₂ measurement were recorded using a T-handled type-E thermocouple sensor (8100-201, LI-COR, United States; accuracy: ± 0.5 %) and a portable five-rod, 0.06 m long frequency domain reflectometry (FDR) probe system (ML2x, Delta-T, United Kingdom; accuracy: ± 1%), respectively. However, CO₂ measurements were not always possible due to technical issues and bad weather conditions, resulting in a total of 666 valid measurements. In addition, a pair of soil CO₂ forced diffusion probes (eosFD, EOSense, United States; accuracy: \pm 40 ppm) were installed near LI-8100A collars from 24 April 2024 to 8 November 2024 (Figure S1). These probes, consisting of a soil node and a reference node, are based on a membrane-based steady-state approach and can measure CO2 flux every 5 minutes (Risk et al., 2011). During this period, the probes continuously monitored CO₂ flux at different slope positions (Figure S1), resulting in a total of 39476 valid flux measurements.

2.3 Temperature, and soil moisture, and water table monitoring

The temporal evolution of soil temperature and moisture along the middle part was monitored using Teros12 sensors (Meter Group, München, Germany; accuracy: ± 0.01 –0.02 m³ m⁻³ for moisture and ± 0.5 °C for temperature), with two replicates per slope position, spaced 5 meters apart (Figure 1a) (Henrion et al., 2025). These sensors recorded data at a depth of 10 cm from 14 October 2022 to 28 October 2024,

every 10 minutes. Between the two replicates of each slope position, a station positioned ~1.4 m above the ground recorded air temperature every ten minutes. Additionally, ten soil temperature data loggers (EL-USB-1-PRO, Lascar, United Kingdom; accuracy: ± 0.2 °C) were installed primarily along two evenly spaced transects parallel to the main slope, at a depth of 10 cm (Figure 1a). These loggers recorded soil temperatures at the same frequency as Teros12 sensors from 21 March 2023 to 8 November 2024. Besides, five Levelogger 5 pressure sensors (Solinst, Georgetown, Canada; accuracy: ± 0.1 %) were placed in PVC pipes to capture pressure at the same topographic positions as the Teros12 sensors (Figure 1a), which was then used to interpret groundwater-level dynamics (Henrion et al., 2025). These probes also recorded at 10-minute intervals, from June 2023 through October 2024.

2.4 Soil sampling and laboratory analysis

After completing all gas sampling campaigns, 33 disturbed soil samples (0-10 cm depth) were collected within LI8100A collars at the five slope positions between 30 July and 15 October 2024. An Emlid Reach RS 2 GPS device with centimeter-level precision was used to record the sampling site locations, using a PPK solution with the Belgian WALCORS network, resulting in a mean lateral positioning error of 1.84 cm across all sites. The samples were stored in a refrigerator until laboratory analysis. A subset of the samples was oven-dried at 80 °C for 24 hours (Dettmann et al., 2021), then crushed and ground into a fine powder for soil organic carbon (SOC) and total nitrogen content (TN) analysis (928 Series, LEGO, United States). Roots and litter were removed using tweezers during the pre-processing procedure. We tested the presence of inorganic carbon of each sample by adding one drop of 10 % HCl but found that no inorganic carbon was present in the samples. A subset of fresh samples was used for root biomass analysis. The fresh soil samples were weighed and placed in a 1 mm sieve, then rinsed with water to collect the roots. The washed roots were dried in an oven at 80 °C for 48 hours and then weighed to calculate their dry biomass.

2.5 UAV data acquisition and imagery processing

During the CO₂ flux monitoring period, we conducted regular UAV flights across the study area to collect high-resolution spatial data (Figure S1). A DJI Matrice 300 RTK was equipped with four different sensors: (i) a Red-Green-Blue (RGB) camera (DJI Zenmuse P1 camera, 35 mm and 45 MP), (ii) a multispectral

camera (MicaSense RedEdge-M camera with five discrete spectral bands: blue (475 nm), green (560 nm), red (668 nm), rededge (717 nm), and near-infrared (842 nm), along with a downwelling light sensor), (iii) a LiDAR scanner (DJI Zenmuse L1, integrated with a 20-MP camera with a 1-inch CMOS sensor) and (iv) a thermal infrared camera (TeAX, featuring FLIR Tau2 cores and ThermalCapture hardware). All the UAV flight missions were carried out around noon (10h00-14h00) and the details of UAV campaigns were presented in support material (Text S1). Similar flight patterns and altitudes were used for the UAV missions as in our previous work (Li et al., 2024). Due to the variable weather conditions in the research field, UAV campaigns were not always feasible. In total, one RGB and one LiDAR dataset collected on 7 June 2023, were used in this study and ten multispectral and ten thermal infrared datasets collected between 13 April 2023 and 13 May 2024 (Figure S1).

2.6 UAV imagery processing

The raw multispectral images were processed in the Pix4D mapper software (Pix4D S.A., Lausanne, Switzerland) to generate reflectance maps (resolution: 6 cm) of the five spectral bands of the study area. We calculated the Normalized Difference Vegetation Index (NDVI) across the 10 maps from the monitoring period (Table \$1). The RGB photos were processed in DJI Terra V4.0.10 (DJI, 2023) to generate an orthomosaic image with a resolution of 1.26 cm. The raw LiDAR data was processed in DJI Terra to provide a Digital Terrain Model (DTM; .tif file) with a resolution of 15 cm. We then calculated the terrain wetness index (TWI) in SAGA GIS 9.2.0 using the formula presented in Table 1. The variables derived from the different types of images and their calculation formula were summarized in Table 1.

Table 1. Orthorectified image, topographical, vegetation index, and land surface temperature maps derived from RGB, LiDAR, multispectral and thermal images.

Index	<u>Definition</u>	<u>Unit</u>	Data source
RGB orthomosaic	Orthorectified image mosaicked from RGB image collection	<u>/</u>	RGB
<u>DTM</u>	Digital Terrain Model, the elevation	<u>m</u>	<u>LiDAR</u>
TWI	Terrain wetness index:	<u>/</u>	<u>LiDAR</u>
	In $(As/\tan(b))$, where As is the specific contributing area and b is the slope angle (i.e.,		

		the rate of change in elevation) in radians.		
	<u>NDVI</u>	Normalized Difference Vegetation Index: (near infrared - red) / (near infrared + red)	7	Multispectral
	<u>LST</u>	Land Surface Temperature	<u>°C</u>	Thermal infrared
263				
1 264	The raw thermal infra	ared video streams were converted into RJPG	images using	ThermoViewer version
265	3.0.26 (TeAX, 2022)). Subsequently, the thermal images were p	rocessed with	the Pix4D mapper to
266	generate land surface	e temperature (LST) maps (resolution: 12 cm	n) <u>. To calibrat</u>	e the LST of each date
267	(Figure 2a), we first	applied linear regressions of temperature obta	ined by came	ra and temperature of 2
268	targets on the ground	(Text S1) to create a correction formula. Nex	t, we mapped	the spatial variations of
269	surface emissivity us	ing the classification-based approach (Li et al.	, 2013; Snyde	r et al., 1998) <u>, based on</u>
270	land cover data from	our previous work (Figure 1b; Li et al. (2024))) and emissiv	ity values of each class
271	from literature (Snyd	ler et al., 1998). Finally, we converted the LS	T to thermal r	adiance using Planck's
272	law, applied an emis	sivity-based correction, and then converted the	ne radiance ba	ack to obtain calibrated
273	LST., which were use	ed for soil temperature mapping (Text S1, Fig	ure S2, Table	S2).
274	The RGB photos we	re processed in DJI Terra V4.0.10 (DJI, 2023	3) to generate	an orthomosaic image
275	with a resolution of 1	.26 cm. The raw LiDAR data was processed in	DJI Terra to p	rovide a Digital Terrain
276	Model (DTM; .tif file	e) with a resolution of 15 cm, which was used	l for generatin	ng daily air temperature
277	maps (Text S1) and to	errain wetness index (TWI) (Text S2). The var	riables derived	l from the four types of
278	images were summar	ized in Table S1.		
279	2.7 Daily soil temper	rature mapping		
280	The linear mixed-ef	fects model was utilized to predict the spa	tial distributi	on of daily mean soil
281	temperature (10 cm	depth) across the landscape from 1 May 202	23 to 30 April	2024. This is because
282	mixed models integra	ate both fixed and random effects, which prov	ide a robust fr	amework for analyzing
283	data with non-indep	pendent structures (Pinheiro and Bates, 20	000) <u>. Daily 1</u>	mean air temperature,

Normalized Difference Vegetation Index (NDVI) and calibrated Land Surface Temperature (LST) were

considered as fixed-effect predictors and monitoring sites were included as random effects. The model

was performed in RStudio (v4.1.2) using the *lmer function* of the *lme4 package* (https://CRAN.R-

284

285

287 *project.org/package=lme4*) and was defined as:

288
$$y_{ij} = \beta_0 + \beta_1 x_{ij} + \dots + \beta_p x_{ij} + b_{0j} + b_{1j} z_{ij} + \dots + \epsilon_{ij}$$
 (1)

- 289 Where:
- 290 y_{ij} is the dependent variable (i.e., soil temperature at 10 cm, unit: °C) for observations i in group
- 291 *i*.
- 292 $\beta_0, \beta_1, \dots, \beta_p$ are fixed-effect coefficients.
- 293 <u>• x_{ij} indicates fixed-effect predictors (independent variables).</u>
- 294 b_{0j} , b_{1j} ,... are random-effect coefficients associated with group j, which account for variability
- 295 <u>across groups.</u>
- 296 z_{ij} indicates predictors associated with random effects.
- 297 ϵ_{ij} is the residual error term.
- Soil temperature data were collected from both Teros 12 sensors and data loggers, as described in Section

 2.3. Air temperature measurements were obtained from five stations positioned at different slope

 locations. The NDVI and calibrated LST estimates were extracted from maps by retrieving values at the

 20 soil temperature sensor sites (Figure 1a). These sites were included as random effects in the model to

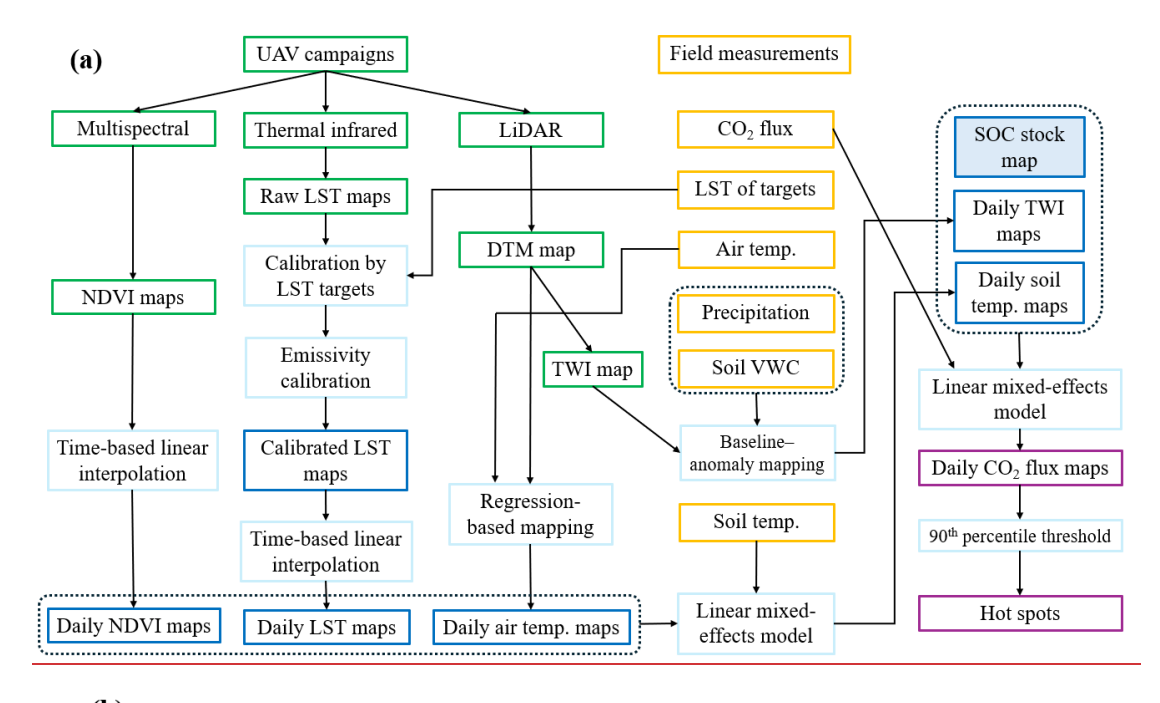
 account for repeated measurements at the same locations throughout the monitoring period. For mapping

 purposes, daily air temperature was statistically downscaled by incorporating the relationship between

 daily air temperature and elevation, followed by downscaling using a Digital Terrain Model (DTM)
- 306 interpolating the monthly/biweekly maps derived from UAVs. The workflow of soil temperature

derived from LiDAR data (Figure 2a). The daily NDVI and LST maps were generated by linearly

307 <u>mapping is illustrated in Figure 2a.</u>



(b) Footslope CO2 flux Backslope 90th percentile Linear mixed-effects Air temp. threshold model Shoulder dry Soil VWC Time series of hourly Shoulder wet CO2 flux Hot moments Topslope Soil temp. Summit

Figure 2. Workflow diagram of daily CO₂ flux spatial mapping (a) and hourly CO₂ flux temporal modeling (b).

312

313

314

315

316

317

318

319

309

310

311

308

2.8 Generation of corrected daily TWI

We generated corrected daily TWI maps to approximate the spatial distribution of daily soil volumetric water content (VWC) by incorporating both long-term site characteristics and daily precipitation effects (Figure 2a). First, we calculated the mean VWC for each site over the period from 1 May 2023 to 30 April 2024. Then, we extracted each site's TWI values from a TWI map generated using the formula in Table 1. Next, we performed a linear regression with mean VWC as the response and TWI as the predictor:

$$Baseline = Mean VWC = b + a * TWI$$
 (2)

The *Baseline* represents the soil moisture level at long-term. A baseline map was then created using this regression model. Daily deviations (anomalies) from the baseline were defined as:

$$Anomaly_t = VWC_{t-} - Baseline$$
 (3)

Considering the memory and lag effects in soil moisture dynamics, we assumed that the anomaly on any

day is influenced by the previous day's anomaly and precipitation:

$$Anomaly_t = c * Anomaly_{t-1} - d * Precipitation_{t-1}$$
 (4)

Finally, we generated a "corrected TWI" map for each day by adding the dynamically updated anomaly to the baseline map:

Corrected
$$TWI_t map = Baseline map + Anomaly_t$$
 (5)

This approach allows the daily corrected TWI maps to capture both the inherent spatial variability (as determined by TWI) and the dynamic influence of rainfall, thereby serving as a proxy for the spatial distribution of soil moisture.

2.96 Statistical analysis

All data analyses were conducted in RStudio (v4.1.2). All timestamps in this study were converted to Coordinated Universal Time (UTC) to ensure consistency across datasets. Group differences were assessed by the *Kruskal-Wallis* test, a non-parametric alternative to the one-way analysis of variance, and suitable for non-normally distributed data (Dunn, 1964). When the *Kruskal-Wallis* test detected a significant overall effect (p < 0.05), *Dunn's* post-hoc test was performed to determine which groups differed significantly from each other, one way analysis of variance (*ANOVA*) using the *stats package*. When *ANOVA* detected a significant effect (p < 0.05), Tukey's Honestly Significant Difference (*HSD*) post-hoc test was performed to determine which groups differed significantly from each other. Pearson correlation analysis was performed using the *corrplot package* (Murdoch and Chow, 1996). The linear mixed-effects models used to identify factors controlling spatial- temporal variations of CO₂ flux, as well as time series simulation and mapping are introduced below.

2.96.1 Models to explain spatial-temporal spatiotemporal variations in CO₂ flux

We <u>also</u> utilized linear mixed-effects model<u>ing framework (i.e., as shown in section 2.7)</u>s to assess the impacts of both static and dynamic environmental factors on the spatial and seasonal variability of CO₂ fluxes. This is because mixed models integrate both fixed and random effects, which provide a robust framework for analyzing data with non-independent structures (Pinheiro and Bates, 2000). The model was performed using the *lmc1* package (Bates et al., 2015), with Unlike the soil temperature model, the natural logarithm of CO₂ flux observations <u>was utilized</u> as a response. The CO₂ fluxes data are often characterized by extreme values and right-skewed distribution, and a lognormal assumption for CO₂ fluxes could better account for the influences of extreme values on the overall distribution (Wutzler et al., 2020). The mixed effects models were defined as:

355
$$y_{ij} = \beta_0 + \beta_1 x_{ij} + \dots + \beta_p x_{ij} + b_{0j} + b_{1j} z_{ij} + \dots + \epsilon_{ij}$$
 (1)

356 Where:

345

346

347

348

349

350

351

352

353

354

357

365

370

371

- y_{tt} is the dependent variable (i.e., ln (CO₂ flux), unit: μmol m⁻² s⁻¹) for observations i in group
- 358
- 359 $\beta_0, \beta_1, \dots, \beta_n$ are fixed effect coefficients.
- 360 x_{tt} is the fixed effect variable (independent variable).
- 361 b_{0j} , b_{1j} ,... are random effect coefficients associated with group j, which account for
- 362 variability across groups.
- 363 z_{tt} is the random effect variable.
- 364 ϵ_{tt} is the residual error term.
 - The fixed-effect predictors were categorized into three groups:
- Static variables: SOC stock, and the ratio of SOC content to nitrogen content (C/N ratio).
- Semi-dynamic variables: root biomass and NDVI.
- Dynamic variables: soil temperature and soil moisture at 0–10 cm depth, as well as water table

 and atmospheric pressure (the latter two variables are shown in the support material).
 - Estimates for NDVI were extracted from the NDVI maps by retrieving the value of the 33 CO₂ flux observation sites and the SOC stock values were extracted from the a local high resolution (0.15 m) SOC stock map (Li et al., 2024). The sites were included as random effects in the seasonal pattern model to

account for repeated measurements at the same locations during the monitoring period, whereas slope positions were treated as random effects in the spatial pattern model. Independent variable coefficients, Intraclass Correlation Coefficient (ICC), coefficients of determination (marginal R² and conditional R²), Root Mean Square Error (RMSE), and Akaike Information Criterion (AIC) were extracted using the modelsummary package after running each model. The ICC quantifies the proportion of variance explained by a grouping (random) factor in multilevel data; values close to 1 indicate high similarity within groups, while values near 0 suggest that grouping conveys little to no information (Nakagawa et al., 2017; Shrout and Fleiss, 1979). The marginal R², represents the variance explained by fixed effects alone, and conditional R² represents the variance explained by both fixed and random effects (Pinheiro and Bates, 2000). The relative importance of each independent variable was obtained using the glmm.hp package(Lai et al., 2023; Lai et al., 2022). To assess multicollinearity in regression analysis, the carpackage was used to calculate the variance inflation factor (VIF) (Fox and Monette, 1992).

2.96.2 Modelling hourly CO₂ flux

The mixed-effects model was utilized to simulate the time series of CO₂ fluxes at different slope positions (Figure 2b). Here, the slope position was included as random variable, and the natural logarithm of CO₂ flux (hourly) was set as a response. We utilized CO₂ fluxes data measured by both the LI8100A system and eosFD probes. Specifically, we randomly selected a number of 30 observations from the eosFD probes at each slope position to reduce data redundancy from high-frequency sampling. Afterwards, we applied weighting to adjust the remaining imbalance in data density between the high-frequency eosFD monitoring and low-frequency LI8100A measurements, ensuring both data sources contributed proportionally to the model. The independent variables included hourly soil temperature (10 cm depth), volumetric soil moisture (VWC, 10 cm depth), and air temperature (1.4 m height), considering their importance in explaining the seasonal and diurnal patterns of CO₂ flux.

As in our previous work (Li et al., 2024), we divided the dataset into a training set (70 %) and a test set (30 %) using K-means clustering to minimize biases that could arise from random sampling (Hair et al., 2010). The models were trained on the training set, and the simulation accuracy was validated using the test dataset. The coefficient of determination (R^2) and RMSE were used to assess the quality of the model fit. Finally, we we made simulations of the time series of hourly CO₂ flux for different slope positions

from 1 May 2023 to 30 April 2024. Furthermore, we identified CO₂ emission hot moments based on the description in Section 2.69.4.

2.96.3 Mapping daily CO2 flux

The linear mixed-effects model was utilized to map the spatial distribution of daily CO₂ fluxes across the landscape, with daily soil temperature (10 cm depth), corrected daily TWI, and SOC stock being considered as fixed-effect variables and gas sampling sites being included as random variables (Figure 2a). The daily CO₂ flux model training, testing procedures, and evaluation of model fit followed the same approach detailed in Section 2.6.2. We then applied the trained model to predicted the daily CO₂ flux of the landscape from 1 May 2023 to 30 April 2024. Additionally, we calculated the mean daily soil CO₂ flux maps for each season and the entire year. Based on these predictions, we identified hot spots for each day by the methods described below.

2.96.4 Quantifying hot moments and hot spots of CO₂ flux

In previous studies, percentiles have been used as thresholds for identifying heat waves (e.g., (Meehl and Tebaldi, 2004): 97.5th percentile), soil heat extremes (e.g., García-García et al. (2023): 90th percentile), hot spots of N₂O emissions (e.g., Mason et al. (2017): median plus three times the interquartile range), and hot spots of CO₂ emissions (e.g., Wangari et al. (2023): median plus the interquartile range). In this study, we tested different methods and selected the 90th percentile as the threshold of both hot moments and hot spots to balance capturing extreme CO₂ emissions while maintaining a sufficient sample size. To capture the hot moments, we calculated a threshold for each slope position separately using its own dataset (Figure 2b). For hot spots, we determined a daily threshold based on each map (Figure 2a).

2.10 Model performance evaluation

Independent variable coefficients, Intraclass Correlation Coefficient (*ICC*), coefficients of determination (*marginal R*² and *conditional R*²), Root Mean Square Error (*RMSE*), and Akaike Information Criterion (*AIC*) were extracted using the *modelsummary* package after running each model described in section 2.7 and section 2.9.1. The *ICC* quantifies the proportion of variance explained by a grouping (random) factor in multilevel data; values close to 1 indicate high similarity within groups, while values near 0 suggest that grouping conveys little to no information (Nakagawa et al., 2017; Shrout and Fleiss, 1979).

The marginal R^2 represents the variance explained by fixed effects alone, and the conditional R^2
represents the variance explained by both fixed and random effects (Pinheiro and Bates, 2000). The
Kling-Gupta Efficiency (KGE) between observations and predictions was also calculated, with values
closer to 1 indicating good model performance (Gupta et al., 2009). The relative importance of each
predictor was obtained using the glmm.hp package (Lai et al., 2023; Lai et al., 2022). To assess
multicollinearity in regression analysis, the car package was used to calculate the variance inflation factor
(VIF) (Fox and Monette, 1992).
For modelling daily soil temperature (i.e., section 2.7) and daily/hourly CO ₂ flux (i.e., sections 2.9.2 and
2.9.3), we divided the corresponding dataset into a training set (70 %) and a test set (30 %) using K-
means clustering, following the methodology of our previous work (Li et al., 2024), to minimize biases
that could arise from random sampling (Hair et al., 2010). The models were trained on the training set,
and the simulation accuracy was validated using the test dataset. The coefficient of determination (R^2) ,
RMSE and KGE were used to assess the quality of all model fits. The daily soil temperature model yielded
R ² , RMSE, and KGE values of 0.89, 1.33 °C, and 0.94, respectively (Figure S2). Detailed results on
model coefficients and performance are summarised in Table S1.

3 Results

445

446

447

448

449

450

451

452

453

454

455

456

457

458

459

460

461

462

463

464

465

466

467

468

469

470

3.1 Peat soil surface and subsurface properties

Table 2 presents an overview of soil surface and subsurface properties at different slope positions. The air temperature above ground ~1.4 m shows great temporal variability, ranging from -8.76 to 24.79 °C within one year. Soil temperatures have smaller temporal variations (0.75 - 17.48 °C), while the mean daily soil temperature (± one standard deviation (SD)) at the topslope (8.86 ± 3.69 °C) is relatively lower than at other positions. Soil volumetric water content (VWC) across the landscape also exhibits significant spatial heterogeneity. The backslope has the highest mean daily VWC ($0.94 \pm 0.04 \text{ cm}^3 \text{ cm}^{-1}$ 3), followed by the footslope $(0.86 \pm 0.06 \text{ cm}^3 \text{ cm}^{-3})$, shoulder wet $(0.85 \pm 0.01 \text{ cm}^3 \text{ cm}^{-3})$, and summit $(0.82 \pm 0.04 \text{ cm}^3 \text{ cm}^{-3})$. The water table at the topslope showed large fluctuations throughout the year (range: -77.41-0.38 cm; mean \pm SD: -21.76 ± 25.17 cm), as shown in Table 2. In contrast, the water table at the shoulder wet slope position remained close to the surface and relatively stable within one year (range: -20.21-4.17 cm; mean \pm SD: -2.17 ± 5.62 cm). No significant differences in dry root biomass were observed among the various slope positions, which may be attributed to substantial small-scale variations within each position, particularly at the shoulder, where the biomass ranged from 0.70 to 8.46 g/100g soil. The SOC content values for summit and shoulder wet areas are 47.38 ± 2.06 g/100g and 47.00 ± 1.41 g/100g, respectively. The SOC content in the shoulder and backslope positions is similar, approximately 42 g/100g, while the carbon content in the footslope and topslope positions is comparatively lower. In addition, the TN content at the topslope $(1.61 \pm 0.48 \text{ g/}100\text{g})$ is significantly lower than at other positions (p < 0.05). The C/N ratio at the footslope (17.41 \pm 1.57) was significantly lower than at the summit, topslope, and backslope (p < 0.05), while no significant differences in C/N ratios were observed among the other places.

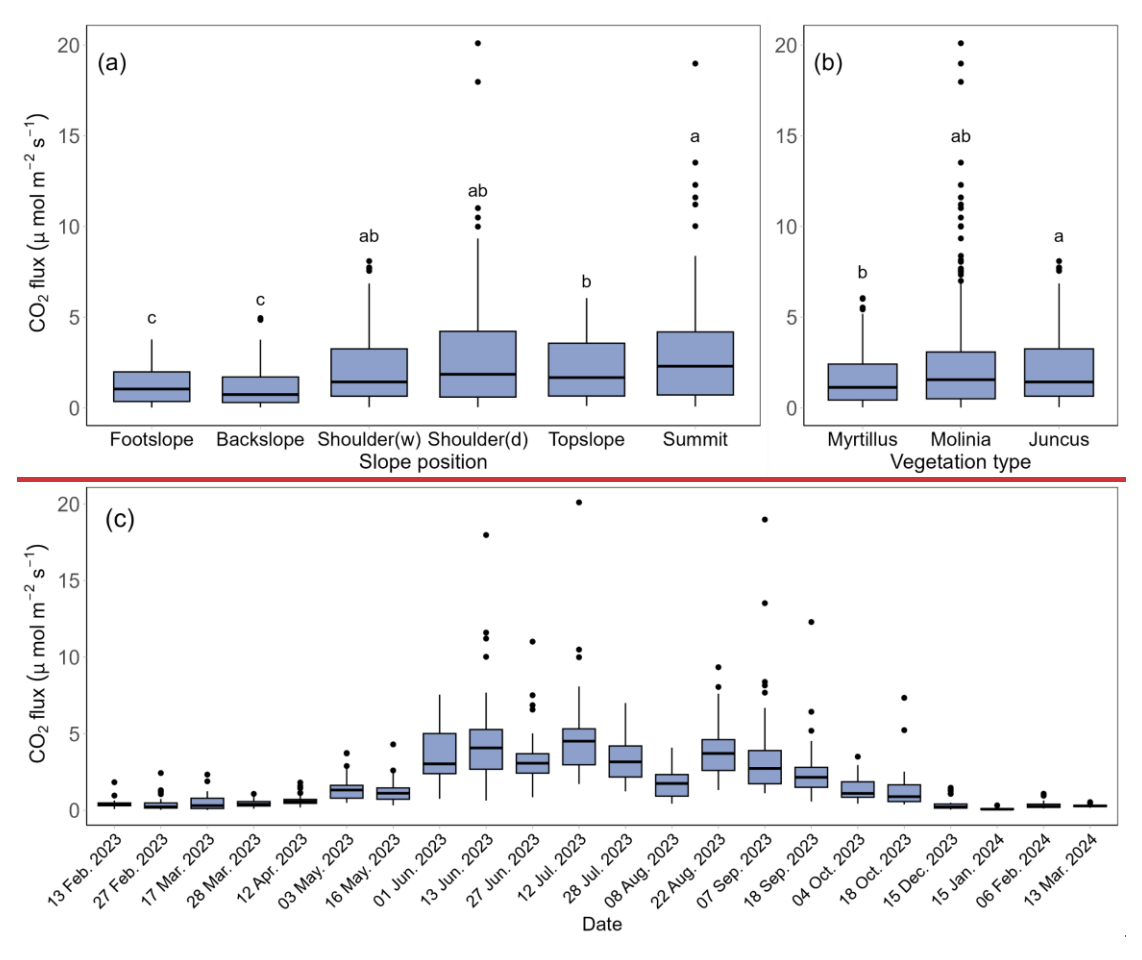
Table 2. Summary of the mean daily air temperature (*Air temp.*), soil temperature (*Soil temp.*), soil volumetric water content (VWC), and water table in one year at different slope positions. Soil subsurface properties at 10 cm depth, i.e, dry root biomass, soil organic carbon (SOC) content, total nitrogen (TN) content, and C/N ratio, at different slope positions.

Slope positions	Footslope	Backslope	Shoulder wet	Shoulder dry	Topslope	Summit
Vegetation	<u>Molinia</u>	<u>Vaccinium</u>	<u>Juncus</u>	<u>Molinia</u>	<u>Vaccinium</u>	<u>Molinia</u>
vegetation	<u>caerulea</u>	<u>myrtillus</u>	<u>acutus</u>	<u>caerulea</u>	<u>myrtillus</u>	<u>caerulea</u>
<u>Air temp.</u> (°C)	9.04 ± 6.79 a (-8.76, 23.75)	9.70 ± 6.77 a (-7.68, 24.79)	9.74 ± 6.73 a (-7.77, 24.60)	<u>N.A.</u>	9.66 ± 6.80 ° (-7.83, 24.66)	9.25 ± 6.89 a (-8.44, 24.52)
Soil temp.	$\frac{9.67 \pm 4.62^{\text{ a}}}{(1.29, 17.48)}$	$\frac{9.55 \pm 4.27^{\text{ ab}}}{(1.40, 16.98)}$	9.65 ± 4.27 a (1.62, 16.74)	$\frac{8.89 \pm 4.15^{\text{ bc}}}{(0.75, 15.52)}$	8.86 ± 3.69 ° (1.55, 15.18)	$\frac{9.18 \pm 4.07}{\text{abc}}$ $\frac{(1.82, 16.00)}{(1.82, 16.00)}$
<u>VWC</u> (cm³ cm⁻³)	$\frac{0.86 \pm 0.06^{\text{ b}}}{(0.68, 0.91)}$	$\frac{0.94 \pm 0.04^{\text{ a}}}{(0.81, 0.98)}$	$\frac{0.85 \pm 0.01}{\underline{s}}$ (0.83, 0.87)	<u>N.A.</u>	$\frac{0.68 \pm 0.08^{e}}{(0.44, 0.73)}$	$\frac{0.82 \pm 0.04^{\text{ d}}}{(0.70, 0.85)}$
Water table (cm)	-27.15 ± 8.31° (-49.14, - 18.53)	$\frac{-21.07 \pm 7.51^{b}}{(-35.91, -9.68)}$	$ \begin{array}{rcl} -2.17 & \pm \\ \underline{5.62^{a}} \\ (-20.21, \\ \underline{4.17}) \end{array} $	<u>N.A.</u>	$\begin{array}{c} -21.76 & \pm \\ \hline 25.17^{d} \\ (-77.41, 0.38) \end{array}$	$ \begin{array}{r} -20.18 & \pm \\ \hline 11.80^{\circ} \\ \hline (-49.23, -9.20) \end{array} $
root biomass (g 100g ⁻¹)	$\frac{1.43 \pm 1.11^{\text{ a}}}{(0.20, 3.37)}$	$\frac{0.97 \pm 0.87^{\text{ a}}}{(0.27, 2.65)}$	4.02 ± 2.10 a (1.98, 6.17)	$\frac{2.97 \pm 3.00^{\text{ a}}}{(0.70, 8.46)}$	$\frac{0.98 \pm 0.99^{\text{ a}}}{(0.18, 2.84)}$	$\frac{0.69 \pm 0.27^{\text{ a}}}{(0.31, 0.96)}$
SOC content (g 100g ⁻¹)	38.48 ± 1.71 b (36.55, 40.80)	$\frac{42.36 \pm 2.46^{\text{ ab}}}{(37.60, 44.30)}$	47.00 ± 1.41 a (45.95, 48.60)	42.53 ± 2.51 ab $(39.75, 45.95)$	$\frac{32.26 \pm 10.81^{b}}{(13.5, 42.1)}$	47.38 ± 2.06 a $(43.95, 49.15)$
TN content (g 100g ⁻¹)	$\frac{2.22 \pm 0.13^{\text{ a}}}{(2.03, 2.37)}$	$\frac{2.02 \pm 0.11^{\text{ ab}}}{(1.89, 2.16)}$	$\frac{2.35 \pm 0.17}{a}$ $\frac{(2.16, 2.47)}{a}$	$\frac{2.04 \pm 0.24^{\text{ ab}}}{(1.71, 2.36)}$	$\frac{1.61 \pm 0.48^{\text{ b}}}{(0.75, 2.19)}$	$\frac{2.13 \pm 0.14^{a}}{(1.99, 2.34)}$
C/N ratio	17.41 ± 1.57 b (15.59, 20.1)	$\frac{20.98 \pm 1.42^{\text{ a}}}{(19.23, 22.70)}$	$ \begin{array}{rcl} 20.03 & \pm \\ 1.26^{\text{ ab}} & \\ (18.81, \\ 21.32) & \\ \end{array} $	$\frac{20.98 \pm 1.95}{a}$ (18.6, 24.06)	$\frac{19.76 \pm 2.01^{\text{ ab}}}{(18.08, 23.36)}$	$ 22.32 \pm 1.79 $ $ (20.21, $ $ 24.51) $

Note. The air temperature was monitored at a height of \sim 1.4 m above the ground. The soil temperature and VWC were monitored at a depth of 10 cm by Teros12 sensors. The results are presented as the mean \pm one standard deviation (SD) and values in brackets indicate the minimum and maximum values. The *Kruskal-Wallis* and *Dunn's* tests were conducted within each class with different superscript letters indicating significant differences (p < 0.05).

3.21 Spatial and temporal Spatiotemporal patterns of CO2 flux

During the monitoring period, the CO₂ emissions show large spatial and seasonal variations across the landscape. The CO₂ fluxes at the summit $(3.16 \pm 3.25 \,\mu\text{mol m}^2\,\text{s}^{-1})$ and shoulder (dry: $2.81 \pm 3.22 \,\mu\text{mol m}^2\,\text{s}^{-1}$), wet: $2.33 \pm 2.36 \,\mu\text{mol m}^2\,\text{s}^{-1}$) slope positions were significantly higher than that of footslope $(1.25 \pm 1.00 \,\mu\text{mol m}^2\,\text{s}^{-1})$ and backslope $(1.11 \pm 1.03 \,\mu\text{mol m}^2\,\text{s}^{-1})$ were significantly lower than that of other slope positions (p < 0.05) (Figure 2a3a). Furthermore, significant differences were observed when grouping the data into three vegetation covers: CO₂ emissions from *Vaccinium myrtillus* were lower than those from *Juncus acutus*, with mean $\pm \,\text{sd} \,\text{SD}$ values of $1.59 \pm 1.43 \,\mu\text{mol m}^{-2}\,\text{s}^{-1}$, and $2.33 \pm 2.36 \,\mu\text{mol m}^{-2}\,\text{s}^{-1}$, respectively (Figure 2b3b) (p < 0.05). However, the CO₂ fluxes under *Molinia caerulea* displayed large variations $(0.02 \sim 20.1 \,\mu\text{mol m}^{-2}\,\text{s}^{-1})$, and no significant differences were found compared to the other two vegetation types. The CO₂ flux data indicated large CO₂ emissions from June to September $(3.65 \pm 2.68 \,\mu\text{mol m}^{-2}\,\text{s}^{-1})$, which can be 8.11 times higher than that from winter and early spring $(0.45 \pm 0.40 \,\mu\text{mol m}^{-2}\,\text{s}^{-1})$ (Figure 2e3c). CO₂ emissions in May and October were at a moderate level.



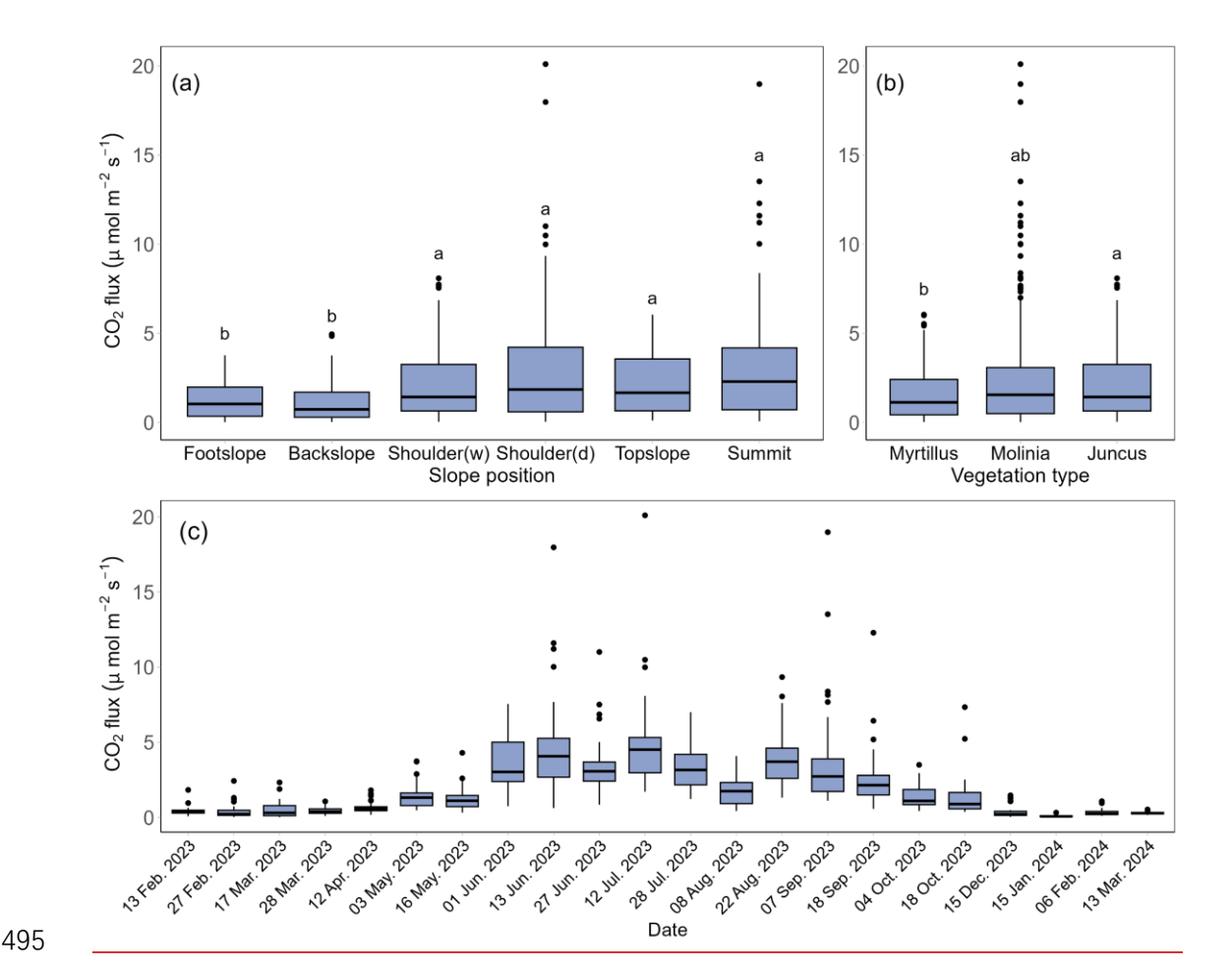
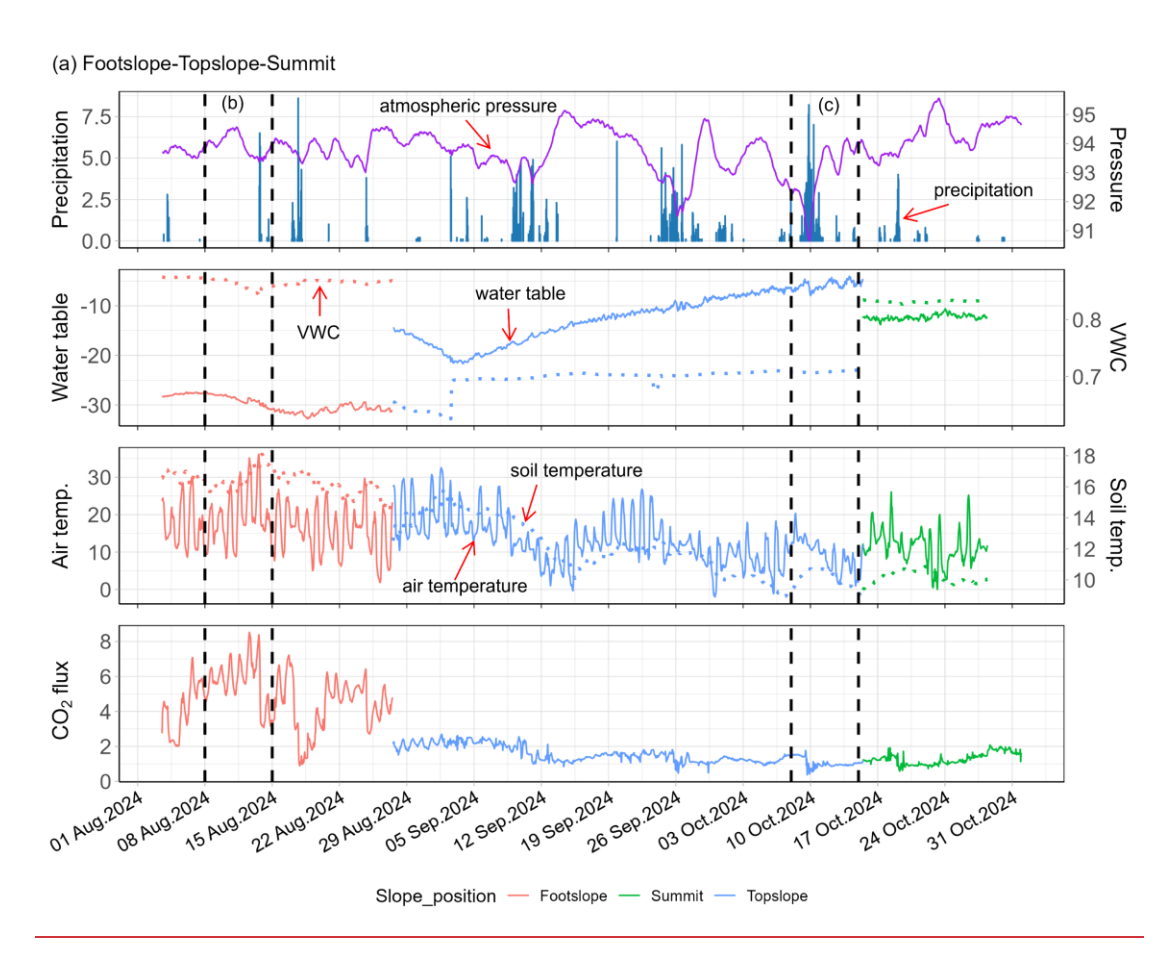


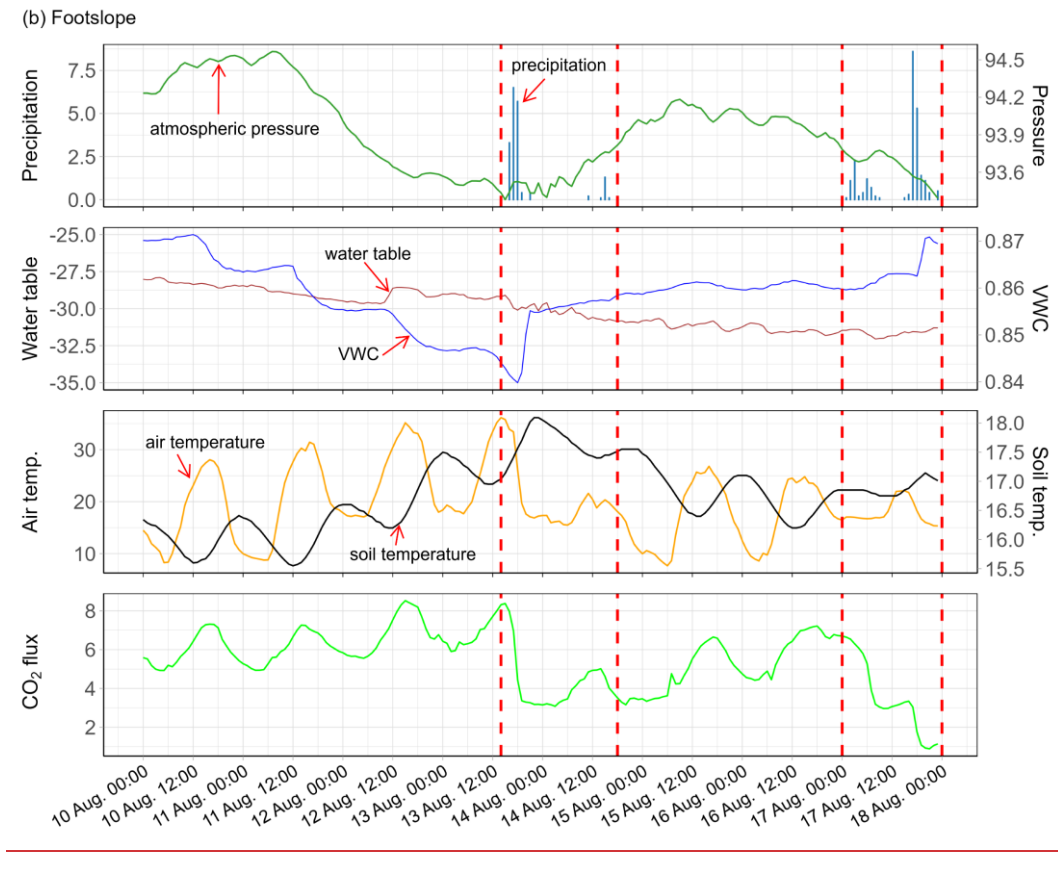
Figure 23. Boxplot of CO₂ flux (μmol m⁻² s⁻¹) across different slope positions (a), vegetation types (b), and sampling dates (c), using data from the LI8100 A system recorded between 2023-02-13 and 2024-03-13. (a), CO₂ flux data of each box were from all dates, and Shoulder (w) and Shoulder (d) indicate shoulder wet and shoulder dry areas, respectively. (b), CO₂ flux data of each box were from all dates, and Myrtillus, Molinia and Juncus indicate *Vaccinium myrtillus*, *Molinia caerulea* and *Juncus acutus*, respectively. (c), CO₂ flux data of each box were from all slope positions. The edges of each box represent the first quartile (Q1) and third quartile (Q3), while the line inside the box indicates the median CO₂ flux. Whiskers extend from the box to the smallest and largest values within 1.5 times the interquartile range, and points outside the whiskers are considered extreme values. The *Kruskal-Wallis* and *Dunn's* tests *ANOVA* and *HSD* post hoc tests were performed within slope positions and vegetation types, with bexes

At the daily scale, the soil respiration displayed a clear diurnal trend from April to August (Figure S3), particularly at the footslope (Figure S3a), backslope (Figure S3b), and shoulder (Figures S3c, 3d) slope positions, with higher CO₂ emissions observed in the late afternoon (14:00–18:00) and lower emissions in the morning (04:00–08:00). In contrast, the diurnal trend of CO₂ flux at the topslope (Figure S3e) and

sharing the same different letters indicating no significant differences among groups (p < 0.05).

summit (Figure S3f) in autumn was less pronounced. Figure 4a presents examples of time series data for CO₂ fluxes and environmental factors at the footslope, topslope, and summit from August to October 2024. In August, clear diurnal patterns with variation magnitudes of 2-3 μmol m⁻² s⁻¹, and reduced CO₂ emissions following precipitation events on 13 August and 17 August were observed at the footslope (Figures 4a, 4b). Since the middle of September, the diurnal variation was less than 1 μmol m⁻² s⁻¹ and there was no obvious pattern in daily changes (Figures 4a, 4c).





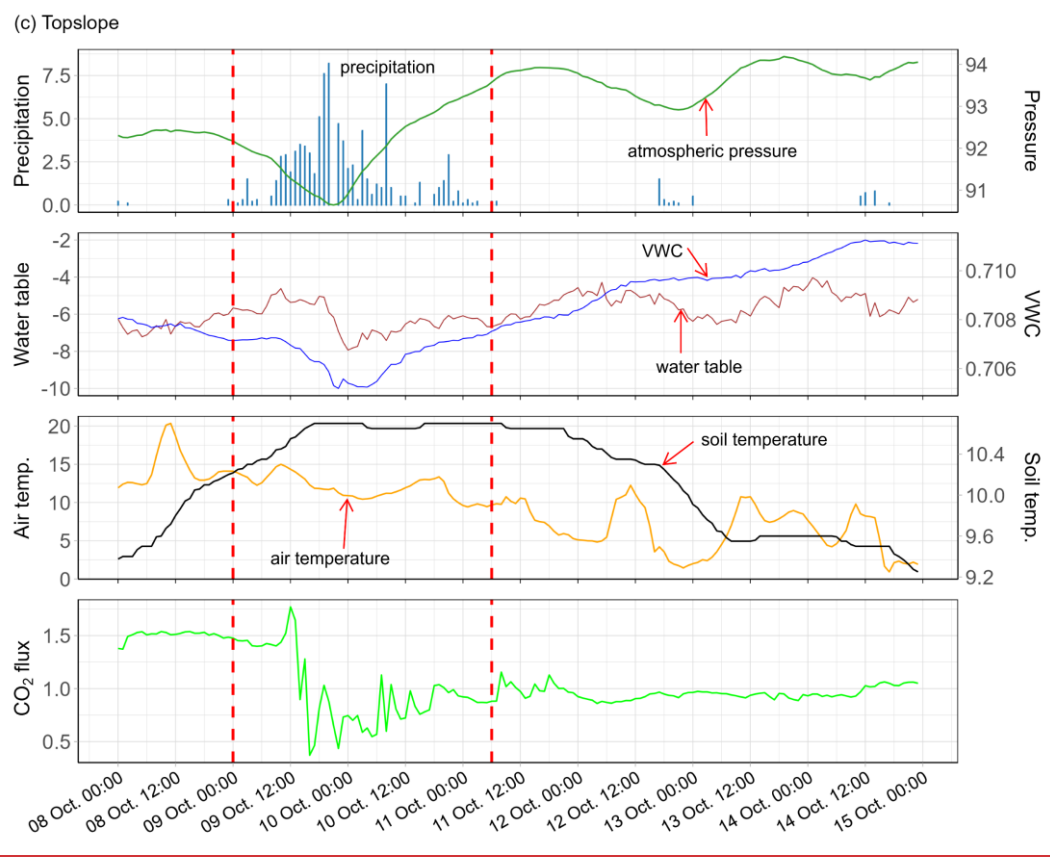


Figure 4. Examples showing time series data of air pressure (kPa), precipitation (mm), soil volumetric water content (VWC, cm³ cm⁻³), water table (cm), soil temperature (Soil temp., °C), air temperature (Air temp., °C), and CO₂ flux

521 (μmol m⁻² s⁻¹, measured by eosFD probes) from 1 August 2024 to 31 October 2024 (a), from 8 August 2024 to 15

August 2024 at the footslope (b), and from 8 October 2024 to 15 October 2024 at the topslope slope position (c).

3.32 Factors contributing to spatial-temporal spatiotemporal variability

Three types of environmental factors explain 64 % of the observed seasonal variance in CO₂ emissions, with contributions of 33 % from soil temperature, 10 % from VWC, 19 % from vegetation (i.e., NDVI, root biomass), 2 % from relatively static factors (i.e., SOC stock, C/N ratio), and 6 % from random effects (i.e., 33 sampling sites) (Table 43). This suggests that long-term stable environmental factors have minimal direct influence on seasonal CO₂ flux patterns. Interestingly, the contribution of these relatively stable factors is nearly 41-6 times higher in explaining overall spatial variations, although soil temperature is still the dominant factor (Table 43). The low *ICC* values in both spatial and seasonal models highlight significant small-scale heterogeneity in soil respiration. Water table contributed 10 % of seasonal variation and atmospheric pressure was not important (1 %), as shown in Table S2 of the support material. The relationships between each environmental factor and CO₂ fluxes are shown in Figure S4.

Table 31. Coefficients and relative contributions of three types of input variables (static, semi-dynamic, dynamic) of mixed linear regression models for modelling CO₂ flux. Random effects were evaluated by *ICC* and model performance was evaluated by *Marginal R*², *Conditional R*², *AIC*, and *RMSE*, and *KGE*.

	Input varial	bles	Seasonal patterns	Spatial patterns
Fixed effects:	Static	SOC stock	0.003	-0.003
coefficient		(t ha ⁻¹)	(1 %)	(0.06 %)
(contribution)		C/N ratio	0.05	0.07*
			(1 %)	(10 %)
	Semi	root biomass	0.06	0.09*
	dynamic	(g 100g ⁻¹)	(0.36 %)	(12 %)
		NDVI	0.90***	-3.35**
			(18 %)	(12 %)
	Dynamic	Soil temp.	0.12***	0.39***
		(°C)	(33 %)	(18 %)
		VWC	-0.77***	-1.37**
		$(cm^3 cm^{-3})$	(10 %)	(11 %)
Random effects	ICC		0.18	0.06
	(contribution	on)	(6 %)	(3 %)
	Marginal R	22	0.64	0.63

Model	Conditional R^2	0.70	0.66
performance	AIC	1386.00	50.10
	RMSE	0.64	0.25
	<u>KGE</u>	0.78	0.78

Note. Significance level: *** p < 0.001, ** p < 0.01, * p < 0.05. All CO₂ fluxes (unit: μ mol m⁻² s⁻¹), soil temperature, and VWC data for spatial and seasonal patterns waswere from the LI8100 A system. To investigate the factors controlling spatial variations of CO₂ flux, we calculated the mean values of CO₂ flux, NDVI, soil temperature, and VWC of each site during the monitoring time.

3.43 Continuous hourly time series of CO₂ flux and hot moments

Three dynamic variables (i.e., soil temp., VWC, air temp.) were taken into account to predict the time series of hourly CO₂ flux at different slope positions. These input variables were selected due to their influential roles in explaining the diurnal (Figure S3, Figure 4) and seasonal (Table 3) fluctuations of CO₂ emissions. As shown in Table 24, the temporal model yielded a robust performance in both training and testing dataset, achieving R^2 and RMSE, and KGE values of 0.86, and 0.39 µmol m⁻² s⁻¹, 0.90, and 0.74 and 0.57 µmol m⁻² s⁻¹, 0.77, respectively.

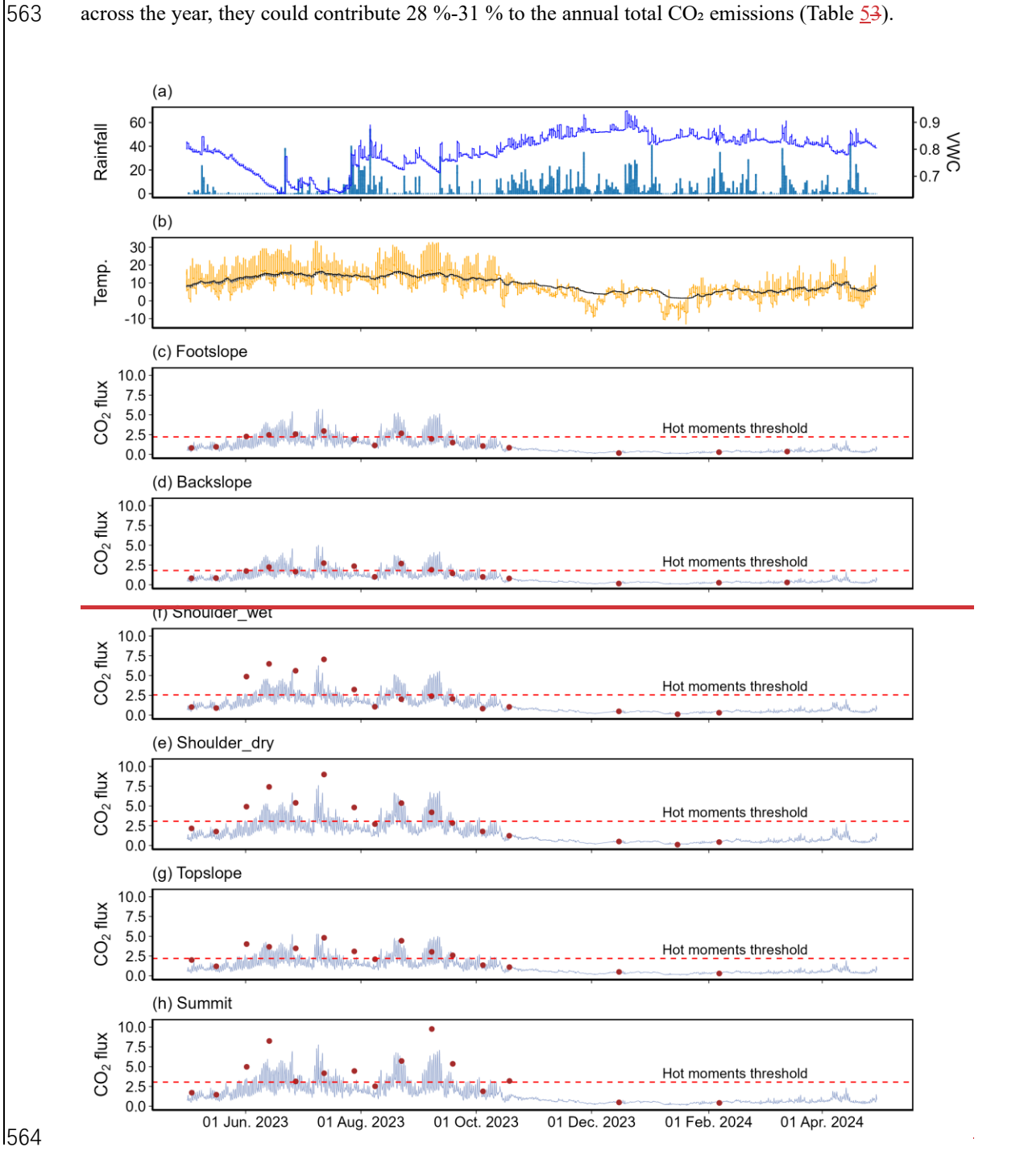
Table 42. Model performance for simulating time series of hourly CO₂ flux (unit: μmol m⁻² s⁻¹) and mapping daily CO₂ flux (unit: μmol m⁻² s⁻¹) across the landscape.

Models	Training dataset			Testing dataset		
Wodels	RMSE	R^2	<u>KGE</u>	RMSE	R^2	<u>KGE</u>
Temporal model	0.39	0.86	0.90	0.57	0.74	0.77
Spatial model	0. 50 49	0.81	<u>0.85</u>	0. 54 <u>56</u>	0.75	<u>0.83</u>

Note. Temporal model used the natural logarithm of CO₂ flux data from LI8100 A and eosFD probes, whereas spatial model used the natural logarithm of CO₂ flux data only from LI8100 A.

The modelled CO₂ emissions at all slope positions display a clear seasonal trend, with higher CO₂ fluxes from June to September and lower estimates in other months, in line with the observed fluxes shown in brown dots (Figures <u>5d3e-5i3h</u>). The total CO₂ fluxes (Table <u>53</u>) at the summit (19.50 t ha⁻¹) and the shoulder (dry: 19.47 t ha⁻¹, wet: 16.31 t ha⁻¹) slope positions were higher than that of topslope (14.45 t ha⁻¹), followed by footslope (13.94 t ha⁻¹) and backslope (11.54 t ha⁻¹) (Table 3), consistent with the spatial patterns of our observations (Figure 3a). However, the modelled mean ± sd CO₂ fluxes at all slope positions (Table 3) were lower than measured CO₂ fluxes by the LI8100 A system. This is because the

measurements were taken during the daytime when fluxes were higher (Figure 2), whereas the modeled values represent the average of both daytime and nighttime fluxes. Most hot moments occurred from June to September 2023, whereas few hot moments were observed from late July to the early August (Figures 5d3e-5i3h). Although these hot moments of different slope positions only accounted for 10 % across the year, they could contribute 28 %-31 % to the annual total CO₂ emissions (Table 53).



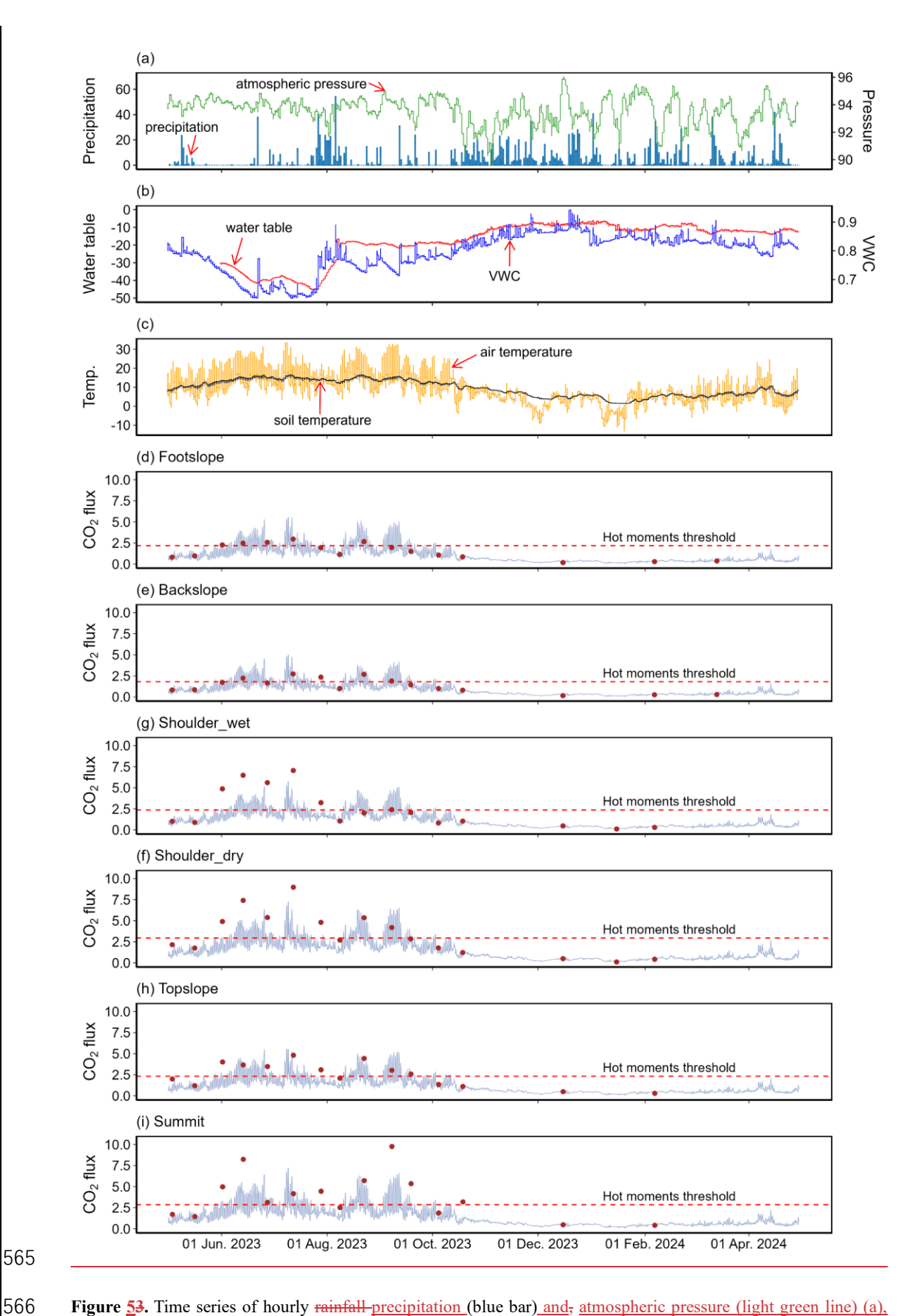


Figure 53. Time series of hourly rainfall precipitation (blue bar) and atmospheric pressure (light green line) (a), hourly mean VWC (blue line) and water table (red line) (ba), hourly mean air temperature (orange line) and soil

temperature (black line) (cb), modelled hourly CO₂ flux (purple lines) and in-situ measurements (brown dots) at different slope positions (de-ih). Precipitation-Rainfall (unit: mm) and atmospheric pressure (kPa) data was from the nearby meteorological observation station (50.51 N, 6.07 E). The water table (cm) data were derived from the Solinist probes. The VWC (unit: cm³ cm⁻³) and soil temperature (unit: °C) were mean values from five slope positions monitored by Teros12 sensors at a depth of 10 cm. Air temperatures (unit: °C) were mean values from 5 stations at 1.4 m height above ground. Measured CO₂ fluxes (unit: µmol m⁻² s⁻¹) were from the LI8100A system.

Table 53. Summary of modelled mean \pm sd-SD CO₂ fluxes, thresholds for identifying hot moments, total CO₂ flux, and the contribution of hot moments to total flux at different slope positions.

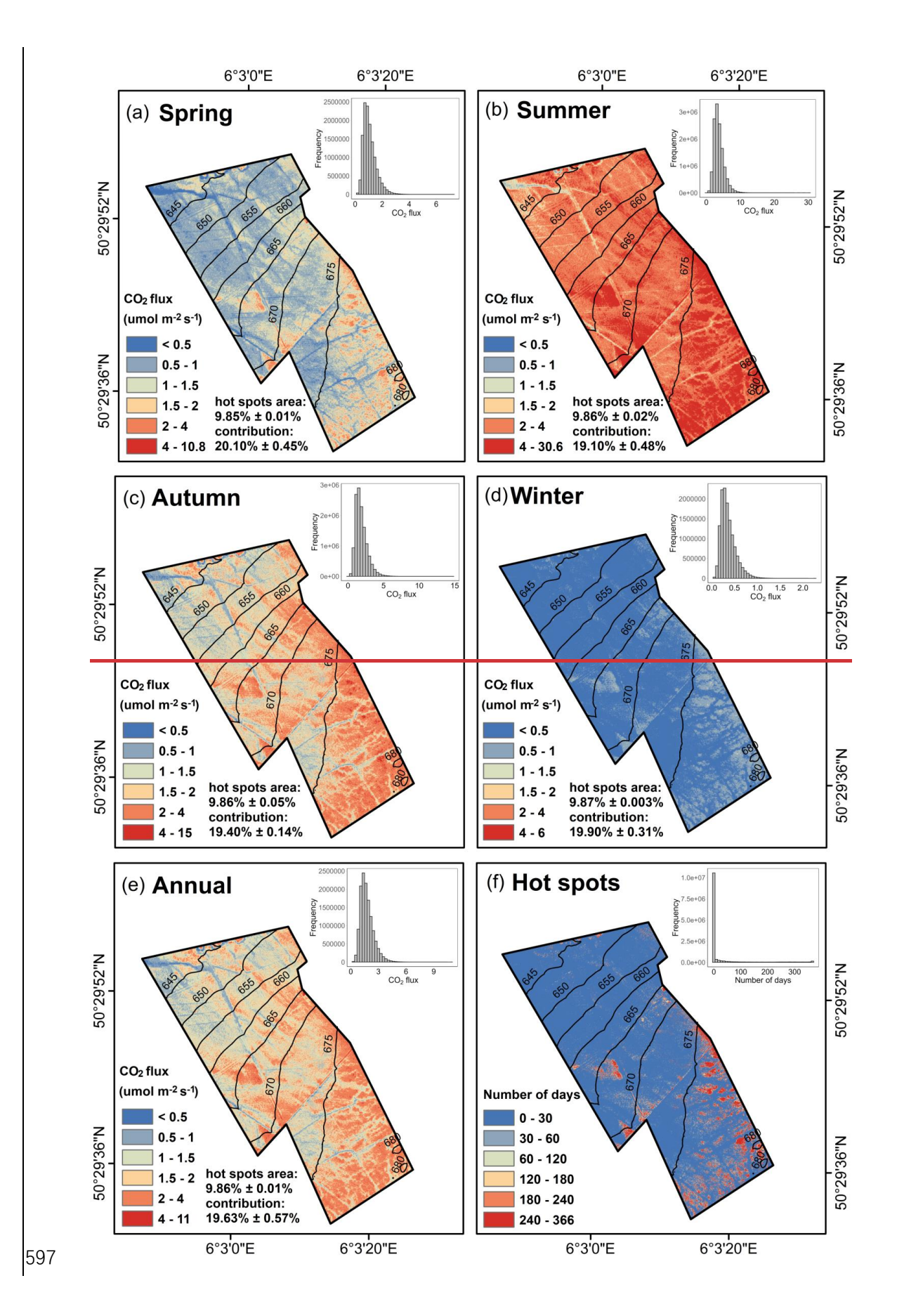
Slope position	Footslope	Backslope	Shoulder	Shoulder	Topslope	Summit
			wet	dry		
Mean ± sd CO ₂ flux	1.00 ± 0.91	0.83 ± 0.73	1.21 ± 0.99	1.44 ± 1.22	1.04 ± 0.86	1.41 ± 1.22
$(\mu mol \ m^{-2} \ s^{-1})$						
Total CO ₂ flux	13.94	11.54	16.31	19.47	14.45	19.50
(t ha ⁻¹)						
Threshold	2.22	1.80	2.55	3.07	2.19	3.04
(µmol m ⁻² s ⁻¹)						
Contribution	30.74 %	30.31 %	28.99 %	28.41 %	28.91 %	29.93 %
of hot moments						

3.54 Daily CO2 flux maps and hot spots

A linear mixed-effects model was utilized to map daily CO₂ flux from 1 May 2023 to 30 April 2024, incorporating soil temperature, corrected TWI, and SOC stock as predictors due to their significant role in explaining the spatial-seasonal variability of CO₂ flux and their availability as spatial data. The mapping model yielded robust performance metrics (Table 24), with *R*², and *RMSE*, and *KGE* values of 0.81, and 0.50 49 μmol m⁻² s⁻¹, and 0.85 in the training dataset, and 0.75, and 0.54 56 μmol m⁻² s⁻¹, and 0.83 in the test dataset, respectively.

Consistent with our observations, the modelled soil respiration also displayed substantial spatial temporal spatial temporal heterogeneity (Figures $\underline{6}4a-\underline{6}4d$). More specifically, the mean CO₂ fluxes ranged from $0.17\underline{0.09}$ μ mol m⁻² s⁻¹- to $10.80\underline{8.23}$ μ mol m⁻² s⁻¹- in spring (Figure $\underline{6}4a$), $0.3\underline{16}$ μ mol m⁻² s⁻¹- to

33.830.60 μ mol m⁻² s⁻¹ in summer (Figure 64b), 0.158 μ mol m⁻² s⁻¹ to 16.884.87 μ mol m⁻² s⁻¹ in autumn (Figure 64c), and 0.034 μ mol m⁻² s⁻¹ to 2.4724 μ mol m⁻² s⁻¹ in winter (Figure 64d). Many modelled mean CO₂ fluxes at the footslope and backslope (elevation < 660 m) remained below 2 μ mol m⁻² s⁻¹ (Figure 64e). In contrast, the modelled CO₂ emissions remained higher throughout the year at the shoulder (660 m \leq elevation \leq 670 m) and east of summit (elevation > 675 m) with high vegetation cover (Figure 1b). About 10 % of the area were identified as hot spots, with a high frequency of hot spots occurring in these regions, while the locations of sporadic hot spots varied over time (Figure 64f). Overall, the landscape emitted approximately 24.34-81 t ha⁻¹ CO₂ to the atmosphere during the simulation period, with $\frac{19.6320.41}{10.6320.41}$ % \pm 0.6157 % of the CO₂ fluxes coming from the hot spots.



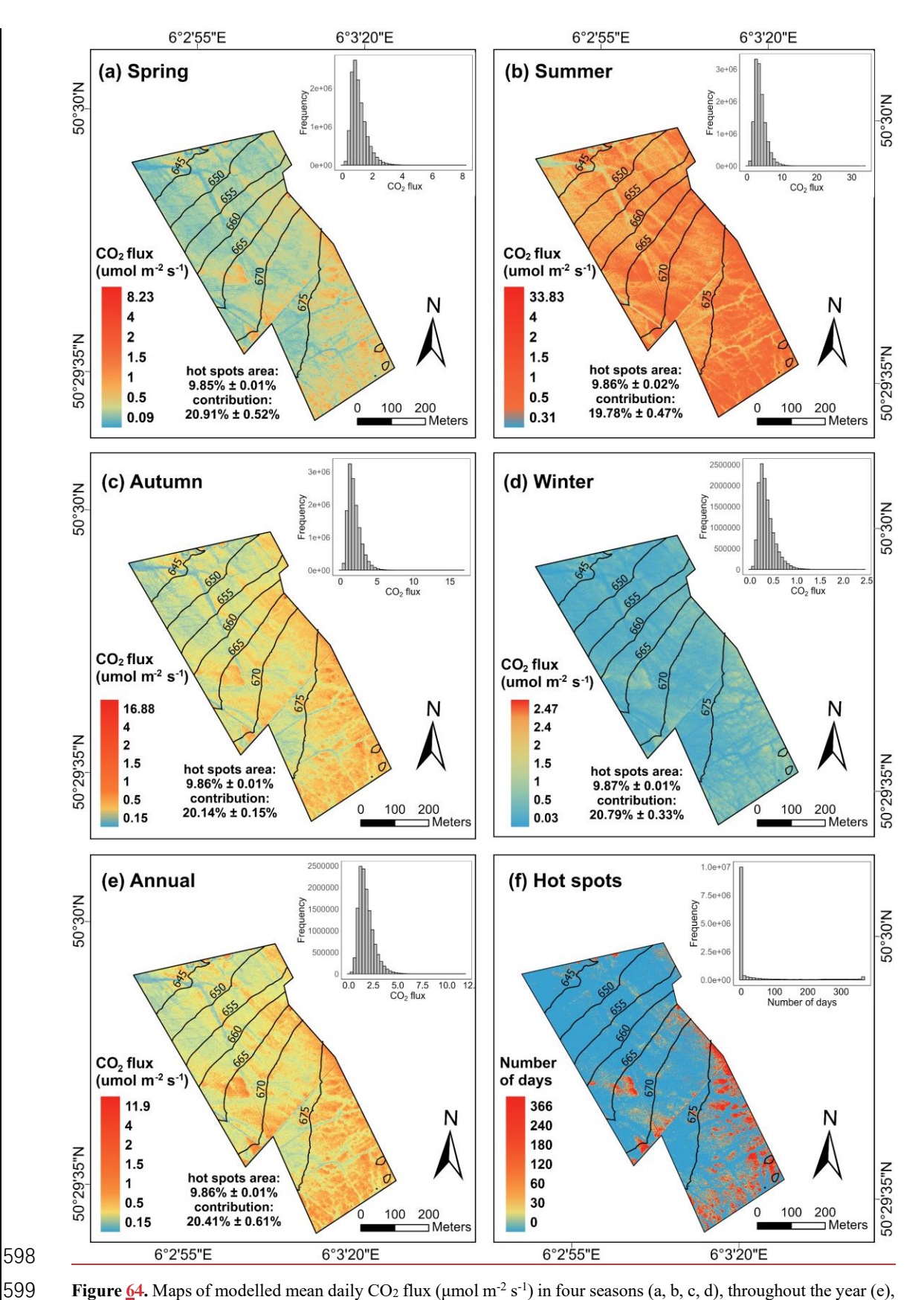


Figure <u>6</u>4. Maps of modelled mean daily CO₂ flux (μmol m⁻² s⁻¹) in four seasons (a, b, c, d), throughout the year (e), and hot spot frequency (f). The histograms of pixel values are presented on the top-right corner of each map. The

- hot spots area proportion and CO_2 flux contribution from the hot spots of each season and across the year are
- summarized in the corresponding maps.

4 Discussion

603

604

605

606

607

608

609

610

611

612

613

614

615

616

617

618

619

620

621

622

623

624

625

626

627

628

629

630

4.1 Drivers of spatiotemporal heterogeneity in CO₂ emission

Consistent with prior temperate peatland studies (Danevčič et al., 2010; Juszczak et al., 2013; Swails et al., 2022; Wilson et al., 2015), our results indicate that seasonal variations in soil CO2 flux across the landscape are highly related to soil temperature, which could account for 33 % of the seasonal variability (Table 13). In contrast to tropical peatlands, where precipitation or water table fluctuations often dominate CO₂ flux dynamics (Cobb et al., 2017; Hoyt et al., 2019), our observations reveal that This relationship is likely due to the influence of temperature on microbial activity, as well as the temperature exhibits distinct seasonal patterns in temperature observed in our study (Figure 53bc), which in turn drive corresponding fluctuations in soil respiration throughout the year (Figure 32c). Moreover, spatial heterogeneity in soil temperature further shaped landscape-scale CO₂ emission patterns (Table 43). For instance, the south-facing summit slopes, which receive more solar radiation in the daytime, consistently show higher CO₂ fluxes (Figure 2n3a). Conversely, the north-facing footslope and backslope, situated on the windward side, experience lower temperatures, resulting in generally lower soil respiration rates throughout the observation period (Figure 32a). At the daily scale, clear soil temperature oscillations were observed in the surface peat, while these diurnal cycles were damped and delayed with depth, with temperature peaks typically occurring at night and valleys around midday (Figures 4, S3). In contrast, the diurnal pattern of soil respiration during growing season (i.e., April to August; Figures 4, S3) was more closely aligned with air temperature, highlighting the important role of air temperature in regulating short-term variations in soil respiration. While temperature is the dominant driver, soilSoil water content influences oxygen availability and nutrients transport within the peat profile, thereby regulating microbial decomposition, plant root activity, and ultimately CO2 production (Deshmukh et al., 2021; Hatala et al., 2012; Huang et al., 2021; Knox et al., 2015; Zou et al., 2022). For example, Knox et al. (2015) demonstrated that a declining water table caused by drainage increases oxygen penetration into the peat, resulting in higher CO2 flux compared to restored peatlands. Previous studies reported nonlinear relationships between soil moisture and soil respiration (Kechavarzi et al., 2010; Marwanto and Agus, 2014; Wood et al., 2013), as both excessively dry and overly saturated conditions can limit microbial decomposition. In our study case, we observed a

negative correlation between soil volumetric water content (VWC) and CO ₂ fluxes (Table 3, Figure S4),
with VWC explaining approximately 10 % of the spatial and seasonal variability in soil respiration (Table
3). This may partially explain the slightly higher CO ₂ fluxes were slightly higher in drier shoulder
positions compared to wetter areas (Figure 32a), and VWC accounted for approximately 10 % of the
spatial seasonal variance in CO2 fluxes (Table 1). Numerous studies have demonstrated that water table
levels play a crucial role on soil respiration (Berglund and Berglund, 2011; Evans et al., 2021; Hoyt et
al., 2019; Knox et al., 2015). For example, Knox et al. (2015) demonstrated that a declining water table
caused by drainage increases oxygen penetration into the peat, resulting in higher CO2 flux compared to
restored peatlands. Our study also observed negative correlations between the water table and CO ₂ fluxes
(Figures 4a, S4), whereas the water table accounted for only 10 % of CO ₂ flux seasonal variations (Table
S2). This relatively modest contribution may be attributed to (i) the limited number of observation sites
(i.e., 5 sites along the hillslope), (ii) short duration of water table monitoring that matched the CO ₂ flux
measurement periods, and (iii) the generally low water table throughout the year (Table 2), particularly
at the footslope, backslope, and summit, where maximum water tables remained > 9 cm below the ground
This maintained aerobic layers that support soil respiration, thereby reducing the influence of water table
fluctuations on CO2 fluxes. Increasing spatial coverage and temporal resolution of water table
observations across the landscape would likely improve our ability to examine its influence on CO2
emissions.
Atmospheric pressure can influence gas fluxes via pressure pumping (Ryan and Law, 2005), and thus we
examined its influence on CO2 emission. However, when atmospheric pressure was included as a
predictor in our model, it only accounted for 1 % of seasonal variability in CO ₂ fluxes (Table S2).
Examination of high-frequency time series data (i.e., hourly CO ₂ flux from the eosFD probes) showed
that at the daily scale, the diurnal pattern of CO ₂ fluxes did not follow atmospheric pressure fluctuation
(Figure 4). At longer time scales, the two variables displayed only weak correlations. Moreover, we
observed that declines in atmospheric pressure were often followed by precipitation events, which in turn
were associated with decreases in both air temperature and CO ₂ flux, or slight CO ₂ fluxes increases
(Figure 4). This suggests that atmospheric pressure may indirectly influence soil respiration by affecting
precipitation patterns, rather than exerting a strong direct control. In saturated peatlands, falling
atmospheric pressure has been shown to trigger methane (CH ₄) shullition by releasing trapped gas

bubbles (Baird et al., 2004; Tokida et al., 2005; Tokida et al., 2007), while in our study site, which is a hillslope where the surface peat remains aerobic most of the time (Table 2), such bubble formation and ebullition are likely minimal. Another contributing factor maybe the limitations of our observations that may have limited our ability to detect short-lived CO₂ flux responses to atmospheric pressure fluctuations. Previous studies have shown that vegetation mediates soil respiration through root respiration, exudates, litter inputs, and rhizosphere priming effects (Acosta et al., 2017; Bragazza et al., 2013; Jovani-Sancho et al., 2021; Walker et al., 2016; Wang et al., 2015a). Root respiration, which is closely linked to plant photosynthetic activity, contributes directly to the overall soil CO₂ fluxes (Crow and Wieder, 2005). In our study, the contribution from root biomass becomes more substantial in the spatial model (i.e., 12 %) than in the seasonal model (< 1 %, Table 3). This discrepancy is likely because root biomass was measured only once during the entire CO₂ monitoring period, thereby missing its seasonal dynamics. The monthly/biweekly NDVI is the second-most influential predictor for CO2 seasonal fluctuations (Table 43), explaining 18 % of variability, as NDVI reveals vegetation phenology during the monitoring period. Accordingly, positive correlation was observed between CO₂ flux and NDVI at the seasonal scale (Table 3, Figure S4). In the spatial-pattern model, however, the annual mean NDVI explained 12 % of the spatial variability in CO₂ fluxes (Table 3) and the relationship became negative (r = -0.29, p = 0.11). This shift in correlation may be due to differences in vegetation structure and composition across the landscape. Slope positions with higher mean NDVI values (i.e., topslope and backslope) are mainly covered by dwarf shrubs (i.e., Vaccinium myrtillus), which exhibit lower CO₂ fluxes compared to other vegetation types (Figure 3b). The lower CO₂ fluxes in dwarf shrub areas are likely associated with their lower root biomass (Table 2). the contribution from root biomass becomes more substantial, together with mean NDVI explaining 24 % of spatial variance. These findings align with previous studies that vegetation mediates soil respiration through root respiration, exudates, litter inputs, and rhizosphere priming effects (Acosta et al., 2017; Bragazza et al., 2013; Jovani Sancho et al., 2021; Walker et al., 2016; Wang et al., 2015a). In our study, the CO2 fluxes of dwarf shrubs (i.e., Vaccinium myrtillus) were significantly lower than those in Juneus acutus-dominated areas (Figure 2b), likely due to the lower root biomass of dwarf shrubs (Table S3). Furthermore, it has been shown that dwarf shrubs in northern peatlands produce highphenolic litter with higher resistance to breakdown and introduce more water-soluble phenolics into the soil compared to Sphagnum moss/herbs (Bragazza et al., 2013; Wang et al., 2015a), which further

660

661

662

663

664

665

666

667

668

669

670

671

672

673

674

675

676

677

678

679

680

681

682

683

684

685

686

687

688

constrains microbial activity and CO₂ production. In addition, vegetation cover may indirectly influence soil respiration by regulating surface microclimate conditions such as humidity and temperature (Nichols, 1998; Stoy et al., 2012).

As shown in Table 34, the SOC stock and C/N ratio have limited explanatory power for the seasonal variability of CO₂ flux, in line with findings of Danevčič et al. (2010). However, when analyzing drivers of average soil CO₂ flux rate across the entire monitoring period, the importance of C/N ratio increased nearly 11 times (Table 34). This likely reflects how long-term averaging integrates short-term dynamic variability, thereby amplifying the role of spatial heterogeneity mediated by the C/N ratio. Prior studies suggesting that the quality of organic material, rather than its quantity, primarily regulates CO₂ fluxes in peatlands (Hoyos-Santillan et al., 2016; Leifeld et al., 2012). Specifically, the soil C/N ratio is known to regulate microbial community functionality and respiration intensity- (Briones et al., 2014; Ishikura et al., 2018; Leifeld et al., 2020; Wang et al., 2015b).

4.2 CO₂ emission hot moments and hot spots: identification, implications, and importance

4.2.1 Temporal analysis and hot moments

During past decades, efforts have been made to model CO₂ flux over time based on its relationship with environmental factors such as hydrology, temperature, substrate quality, microbial community, and vegetation (Abdalla et al., 2014; Anthony and Silver, 2021; Farmer et al., 2011; Hoyt et al., 2019; Junttila et al., 2021; Rowson et al., 2012; Schubert et al., 2010).- In our study, diurnal cycles of CO₂ fluxes are closely related to air temperature (Figure 4, Figure S3), while soil temperature and moisture are important factors in explaining the seasonal patterns of CO₂ flux (Table 34). Hence, the three dynamic environment variables were incorporated into the model to simulate the hourly CO₂ flux across the entire monitoring period. Overall, the temporal model demonstrated robust performance in both the training and testing datasets (Table 42) and effectively captured seasonal and diurnal trends at most sites (Figures 53de-5i3h). However, the modelled peak values are lower than the observations at shoulder and summit slope positions (Figures 3f5g, 3e5f, 3h5i), which may be partially due to the limited number of high-value observations in these areas. Consequently, the model is more influenced by the more frequent lower CO₂ fluxes, leading to an overall underestimation of the peak. -In addition, two types of gas analyzers were

employed to monitor CO₂ flux with different sampling frequency and time: the LI-8100A sensor was used biweekly or monthly to capture seasonal trends, while eosFD probes collected data every five minutes to track diurnal fluctuations. The integration of these datasets for modelling temporal dynamics improved estimation accuracy but might also introduce uncertainties into the model.

716

717

718

719

720

721

722

723

724

725

726

727

728

729

730

731

732

733

734

735

736

737

738

739

740

741

742

743

Anthony and Silver (2023) demonstrated that identifying hot moments of CO₂ flux in peatland requires intensive continuous measurements, while as an alternative, our robust simulation of hourly CO2 flux enabled the identification of hot moments in a complex landscape. We found that most of these hot moments occurred during the summer and early autumn seasons (Figures 3e5d-3h5i), in agreement with our in-situ observations (Figure 2e3c). The frequent high CO₂ emissions in June and July can be attributed to the low precipitation and water table level, decreased soil moisture, and high temperatures (Figures 3a5a-3b5c). In water-limited ecosystems or during the dry season of tropical peatlands, precipitation pulses can trigger hot moments of CO₂ gas emissions, as precipitation regulates soil moisture and infiltrating water physically displaces CO₂ from soil pores (Fernandez-Bou et al., 2020; Leon et al., 2014; Wright et al., 2013). This occurs when rainwater rapidly infiltrates dry soil, filling airfilled pores and forcing CO2-rich air out due to hydraulic pressure. However In this study, CO2 fluxes showed both decreases and increases in response to precipitation events (Figure 4). few hot moments were captured during late July and early August due to the heavy rainfall events (Figure 3a). Theis absence observed decreases may be attributed to the high water content of the surface peat, and prolonged and fact that intense rainfall led to lower temperatures, and increased soil moisture, and higher water table (Figures 4, 3a5b, 3b5c), thereby suppressing microbial and root respiration (Hoyt et al., 2019). Consequently, a few hot moments were captured during late July and early August during the heavy rainfall events (Figure 5). Following this period, CO₂ emissions reached values that exceeded the 'hot moments' threshold in mid-August, aligning with declining rainfall and rising temperatures (Figures 3e5d-3h5i). The hot moments observed in September are linked to seasonal fluctuations in atmospheric pressure, precipitation, water table, and temperature (Figures 3a5a-5c,3b).

Similar to the findings of Anthony and Silver (2021) and Kannenberg et al. (2020), these hot moments accounted for approximately 10 % throughout the year, while they contributed significantly to the annual total CO₂ emissions (28 %-31 %; Table 3), highlighting the important role of short-term high-emission

events in the overall carbon emission. Therefore, missing hot moments may lead to significant underestimates of total peat soil respiration budgets. Despite continuous automated chamber or eddy covariance measurements that are ideal for capturing hot moments of CO₂ emissions (Anthony and Silver, 2021; Anthony and Silver, 2023; Hoyt et al., 2019), long-term continuous monitoring is still labor-intensive and cost-prohibitive in many locations within the complex peatland ecosystems. Given that we observed a concentration of hot moments in the summer and autumn, we recommend increasing monitoring frequency during these seasons for temperate peatlands. This strategy would help capture carbon emission dynamics more effectively, reduce uncertainties in annual carbon flux estimates, and provide more representative peatland CO₂ flux data.

4.2.2 Spatial analysis of CO₂ fluxes and hot spots

744

745

746

747

748

749

750

751

752

753

754

755

756

757

758

759

760

761

762

763

764

765

766

767

768

769

770

771

Our mapping of daily CO₂ flux across the landscape yielded a model performance of $R^2 = 0.75$, KGE = 0.83, and RMSE = 0.564 µmol m⁻² s⁻¹ for the test dataset (Table 42). This can be attributed to the incorporation of key environmental factors that drive the spatiotemporal heterogeneity of soil respiration into the model inputs. These factors – including soil temperature, corrected TWI, and SOC stock – can be directly obtained through multi-sensor UAV remote sensing or estimated using high spatiotemporal resolution <u>UAV</u> data. Previous studies upscaled spatial carbon fluxes using area-weighted methods, extrapolating point data from CO₂ chamber flux measurements to adjacent or larger areas based on land cover maps (Leon et al., 2014; van Giersbergen et al., 2024; Webster et al., 2008). However, this approach can lead to over- or underestimation (Leifeld and Menichetti, 2018; Wangari et al., 2023), because our findings reveal that even within the same vegetation cover, such as Molinia caerulea, CO2 emissions exhibit significant spatial temporal variability (Figure 32b). In recent years, spatial upscaling of CO₂ fluxes has increasingly relied on satellite-based remote sensing data (e.g., Azevedo et al. (2021); Huang et al. (2015); Junttila et al. (2021); Wangari et al. (2023); Zhang et al. (2020). -While this method covers larger areas, it is often constrained by coarse temporal and spatial resolutions. The peatland ecosystem is characterized by great temporal and spatial heterogeneity at small scales, and ignoring these variations can introduce significant uncertainties in CO₂ emission estimates. Our study demonstrates that multi-sensor and multi-date UAV remote sensing has great potential inhigh resolution UAV remote sensing imagery, with fine temporal and spatial scales, could effectively upscalmodelinge

772 CO₂ fluxes from point measurements across a heterogeneous landscape with high resolution (i.e., spatial: 773 15 cm; temporal: daily interval), thereby reducing uncertainties in spatioal temporal predictions of CO₂ 774 fluxes. 775 However, the key environmental variables used for mapping soil respiration were estimated by UAV data, 776 which inevitably introduce uncertainties into the prediction processes. For instance, because daily UAV 777 imagery was unavailable, the predictors (i.e., air temperature, LST, and NDVI) for modelling the 778 spatiotemporal dynamics of soil temperature were linearly interpolated between acquisition dates, 779 potentially adding uncertainty to the model results. Moreover, flight conditions and preprocessing of the 780 raw UAV data (e.g., georeferencing, resampling, the calibration of LST, downscaling air temperature) 781 may have further introduced errors into the soil temperature estimates. The corrected daily TWI maps 782 were also subject to uncertainty, as they relied on in-situ soil VWC observations, which were only 783 available in the middle transect of the landscape. Similarly, uncertainties in SOC stock mapping arose 784 from the peat thickness estimation and soil sampling strategy, as discussed in our previous work (Li et 785 al., 2024). 786 Furthermore Nevertheless, these reliable high-resolution CO₂ flux maps allowed for the identification of 787 hot spot areas across the landscape. We found that most of the hot spots occurred toat the west of shoulder 788 areas where soil moisture was relatively lower and to the east of the summit which is covered by dense 789 vegetation (Figure 1b, Figure 4f6f). Some sporadic hot spots were found at the backslope and footslope 790 positions. Spatial variability in the factors controlling biogeochemical processes, such as soil temperature, 791 moisture, water table depth, vegetation type, and substrate quality, is likely driving these differences 792 (Anthony and Silver, 2023; Kuzyakov and Blagodatskaya, 2015; McNamara et al., 2008). For instance, 793 the persistent hot spots that occurred at the shoulder might be due to their relatively drier conditions and 794 higher carbon stocks compared to other areas (Li et al., 2024). The tree-covered areas at the summit 795 likely contribute substantial root respiration, which could sustain hot spot formationmay, in turn, trigger 796 the formation of consistent hot pots throughout the year. Besides, litterfall beneath trees insulates the peat 797 soil and provides an abundant resource for microbial activity even during the non-growing season. While 798 at other places, such as the footslope and backslope, which are mainly covered by dwarf shrubs and 799 Molinia caerulea (Figure 1b) with pronounced seasonal phenology, they potentially form sporadic soil

respiration hot spots at specific times of the year. Furthermore, surface peat beneath relatively short vegetation can receive higher direct solar radiation in summer, leading to elevated soil temperatures and the emergence of carbon emission hot spots.

High-emission events from hot spots play a crucial role in overall CO₂ fluxes (Anthony and Silver, 2023), hence, neglecting these areas could lead to substantial underestimation of peatland carbon emissions. In our study, although less than 10 % of area was identified as hot spots, their CO₂ flux contribution accounted for nearly 20 % across the year (Figure 46). However, research specifically focusing on peatland CO₂ emission hot spots remains limited (Anthony and Silver, 2023), despite increased exploration of greenhouse gas emission hot spots in other ecosystems (e.g., agricultural field (Krichels and Yang, 2019; Leifeld et al., 2020; Rey-Sanchez et al., 2022); wetland (Rey-Sanchez et al., 2022); water-limited Mediterranean ecosystem (Leon et al., 2014); forest (Wangari et al., 2023)). Hence, to improve the accuracy of CO₂ spatial budgeting for peatlands, there is a need for enhanced high-resolution dynamic monitoring of hot spot areas (Becker et al., 2008). Our study demonstrates the great potential of UAV technology for peatland hot spot identification and quantification, offering new insights into studying soil respiration within heterogeneous ecosystems as well as optimizing peatland management and CO₂ emission reduction strategies.

5 Conclusion

817

818

819

820

821

822

823

824

825

826

827

828

829

830

831

832

833

834

835

836

837

838

839

840

841

842

843

844

In this study, we monitored the dynamics of peatland surface and subsurface environments using both field surveys and multi-sensor UAVs at high spatial temporal spatiotemporal resolution. We investigated the influence of dynamic and static environmental factors on soil respiration rates across different scales, thereby enhancing our understanding of peatland carbon cycling. Additionally, we simulated CO₂ flux with high spatial temporal resolution by integrating field measurements and UAV data. These reliable modelling allow us to identify and quantify CO₂ emission hot spots and hot moments across the landscape. To summarize, the main findings of our study are as follows: (1) Soil respiration rates vary significantly across space and time, influenced by both dynamic and relatively static environmental factors at different scales. Temperature is the primary driver of CO2 flux variations, explaining 33 % CO₂ seasonal variability and 18 % spatial variability. Soil moisture negatively affects both seasonal and spatial variations, accounting for 10 % - 11 % of the variance. Water table dynamics also play a role (10 %), but more observations are needed to explore its influence. Atmospheric pressure may indirectly influence soil respiration by affecting precipitation patterns, rather than exerting a strong direct control. Semi-dynamic factors (i.e., NDVI and root biomass) contribute 19 % to seasonal variability and 24 % to spatial variability. While relative static factors (i.e., the C/N and SOC stock) have little impact on the seasonal CO₂ flux variability, the contribution of the C/N ratio increases nearly 11 times for spatial variability. (2) Predicting temporal series of hourly CO_2 flux can be effectively achieved (test set: $R^2 = 0.74$, RMSE = $0.57 \mu mol m^{-2} s^{-1}$, KGE = 0.77) by considering its relationship with key environmental variables such as air temperature, soil temperature and soil moisture, all of which are relatively straightforward to monitor. These reliable time series data provide a foundation for capturing respiration pulses occurring over short periods, with hot moments primarily occurring in summer and early autumn. (3) The UAV remote sensing offers great potential in monitoring and estimating key environmental variables that control soil respiration across heterogeneous landscapes. Our model using UAV-derived data predictors can yielded robust spatial mapping of soil respiration rates across heterogeneous landscapes, with RMSE, KGE, and R² values of 0.54-56 µmol m⁻² s⁻¹, 0.83, and 0.75 in the test dataset, respectively. These high-resolution CO₂ flux maps enable us to locate hot spots as well as providing a

845	valuable tool for assessing peatland management strategies, such as evaluating conditions before and
846	after restoration.
1 847	(4) Despite representing 10 % of time within one year, CO ₂ fluxes from hot moments contribute 28 %-
848	31 % to the overall CO ₂ flux budgets. Approximately 10 % areas are identified as hot spots, while
849	contributing $\underline{20.41}\underline{19.63}$ % \pm 0.57- $\underline{61}$ % of total CO ₂ fluxes. The locations of high-frequency hot spots
850	remain consistent, while the locations of sporadic hot spots vary over time.
851	Code and data availability
852	The field measurements of CO ₂ fluxes, climate data, and soil properties are available on <i>HydroShare</i> :
853	https://www.hydroshare.org/resource/a4efce8d4d114b939f0d92a18b3168c6/.
854	Code and UAV data will be made available on request.
855	
856	CRediT authorship contribution statement
857	YL: Writing – original draft, Visualization, Investigation, Formal analysis, Conceptualization. MH:
858	Writing – review & editing, Investigation. AM: Writing – review & editing. SL: Writing – review &
859	editing, Funding acquisition, Conceptualization. SO: Writing – review & editing, Funding acquisition,
860	Conceptualization. VV: Writing – review & editing, Funding acquisition, Conceptualization. FJ: Writing
861	- review & editing, Funding acquisition, Supervision, Conceptualization. KVO: Writing - review &
862	editing, Investigation, Funding acquisition, Supervision, Conceptualization.
863	
864	Declaration of Competing Interest
865	The authors declare that they do not have any commercial or associative interest that represents a conflict
866	of interest in connection with the work submitted.
867	
868	Acknowledgements
869	Yanfei Li wishes to thank the joint grant from China Scholarship Council and UCLouvain (No.
870	202106380030). Kristof Van Oost, Sophie Opfergelt, and Sébastien Lambot are supported by the Fonds
871	de la Recherche Scientifique (FNRS). The authors would like to thank the Département de la Nature et

872	des Forêts (DNF) and Joël Verdin for giving access to the study site. The authors would like to thank
873	Dylan Vellut for his assistance with soil respiration measurements and UAV campaigns.
874	
875	Financial support
876	This work is an Action de Recherche Concertée, n° 21/26–119, funded by the Communauté française

878 References

- 879 Abdalla, M., Hastings, A., Bell, M.J., Smith, J.U., Richards, M., Nilsson, M.B., Peichl, M., Löfvenius, M.O.,
- 880 Lund, M., Helfter, C., Nemitz, E., Sutton, M.A., Aurela, M., Lohila, A., Laurila, T., Dolman, A.J., Belelli-
- 881 Marchesini, L., Pogson, M., Jones, E., Drewer, J., Drosler, M., Smith, P., 2014. Simulation of CO2 and
- Attribution Analysis at Six European Peatland Sites Using the ECOSSE Model. Water, Air, & Soil Pollution,
- 883 225, 2182. 10.1007/s11270-014-2182-8
- 884 Acosta, M., Juszczak, R., Chojnicki, B., Pavelka, M., Havránková, K., Lesny, J., Krupková, L., Urbaniak, M.,
- 885 Machačová, K., Olejnik, J., 2017. CO2 Fluxes from Different Vegetation Communities on a Peatland
- 886 Ecosystem. Wetlands, 37, 423-435. 10.1007/s13157-017-0878-4
- 887 Anthony, T.L., Silver, W.L., 2021. Hot moments drive extreme nitrous oxide and methane emissions from
- agricultural peatlands. Global Change Biology, 27, 5141-5153. https://doi.org/10.1111/gcb.15802
- 889 Anthony, T.L., Silver, W.L., 2023. Hot spots and hot moments of greenhouse gas emissions in agricultural
- 890 peatlands. Biogeochemistry. 10.1007/s10533-023-01095-y
- 891 Arias-Navarro, C., Díaz-Pinés, E., Klatt, S., Brandt, P., Rufino, M.C., Butterbach-Bahl, K., Verchot, L.V., 2017.
- 892 Spatial variability of soil N2O and CO2 fluxes in different topographic positions in a tropical montane
- 893 forest in Kenya. Journal of Geophysical Research: Biogeosciences, 122, 514-527
- 894 https://doi.org/10.1002/2016JG003667
- 895 Azevedo, O., Parker, T.C., Siewert, M.B., Subke, J.-A., 2021. Predicting Soil Respiration from Plant
- 896 Productivity (NDVI) in a Sub-Arctic Tundra Ecosystem, Remote Sensing.
- 897 Baird, A.J., Beckwith, C.W., Waldron, S., Waddington, J.M., 2004. Ebullition of methane-containing gas
- 898 bubbles from near-surface Sphagnum peat. Geophysical Research Letters, 31.
- 899 https://doi.org/10.1029/2004GL021157
- 900 Bates, D., Mächler, M., Bolker, B., Walker, S., 2015. Fitting Linear Mixed-Effects Models Using Ime4. Journal
- 901 of Statistical Software, 67, 1 48. 10.18637/jss.v067.i01
- 902 Becker, T., Kutzbach, L., Forbrich, I., Schneider, J., Jager, D., Thees, B., Wilmking, M., 2008. Do we miss the
- hot spots? The use of very high resolution aerial photographs to quantify carbon fluxes in peatlands.
- 904 Biogeosciences, 5, 1387-1393. 10.5194/bg-5-1387-2008
- 905 Berglund, Ö., Berglund, K., 2011. Influence of water table level and soil properties on emissions of
- 906 greenhouse gases from cultivated peat soil. Soil Biology and Biochemistry, 43, 923-931.
- 907 https://doi.org/10.1016/j.soilbio.2011.01.002
- 908 Bragazza, L., Parisod, J., Buttler, A., Bardgett, R.D., 2013. Biogeochemical plant-soil microbe feedback in
- 909 response to climate warming in peatlands. Nature Climate Change, 3, 273-277. 10.1038/nclimate1781
- 910 Briones, M.J.I., McNamara, N.P., Poskitt, J., Crow, S.E., Ostle, N.J., 2014. Interactive biotic and abiotic
- 911 regulators of soil carbon cycling: evidence from controlled climate experiments on peatland and boreal
- 912 soils. Global Change Biology, 20, 2971-2982. https://doi.org/10.1111/gcb.12585
- 913 Bubier, J.L., Bhatia, G., Moore, T.R., Roulet, N.T., Lafleur, P.M., 2003. Spatial and Temporal Variability in
- 914 Growing-Season Net Ecosystem Carbon Dioxide Exchange at a Large Peatland in Ontario, Canada.
- 915 Ecosystems, 6, 353-367. 10.1007/s10021-003-0125-0
- 916 Cobb, A.R., Hoyt, A.M., Gandois, L., Eri, J., Dommain, R., Abu Salim, K., Kai, F.M., Haji Su'ut, N.S., Harvey,
- 917 C.F., 2017. How temporal patterns in rainfall determine the geomorphology and carbon fluxes of tropical
- 918 peatlands. Proceedings of the National Academy of Sciences, 114, E5187-E5196.
- 919 10.1073/pnas.1701090114
- 920 Crow, S.E., Wieder, R.K., 2005. SOURCES OF CO2 EMISSION FROM A NORTHERN PEATLAND: ROOT

- 921 RESPIRATION, EXUDATION, AND DECOMPOSITION. Ecology, 86, 1825-1834. https://doi.org/10.1890/04-
- 922 1575
- 923 Danevčič, T., Mandic-Mulec, I., Stres, B., Stopar, D., Hacin, J., 2010. Emissions of CO2, CH4 and N2O from
- 924 Southern European peatlands. Soil Biology and Biochemistry, 42, 1437-1446.
- 925 https://doi.org/10.1016/j.soilbio.2010.05.004
- 926 Deshmukh, C.S., Julius, D., Desai, A.R., Asyhari, A., Page, S.E., Nardi, N., Susanto, A.P., Nurholis, N.,
- 927 Hendrizal, M., Kurnianto, S., Suardiwerianto, Y., Salam, Y.W., Agus, F., Astiani, D., Sabiham, S., Gauci, V.,
- 928 Evans, C.D., 2021. Conservation slows down emission increase from a tropical peatland in Indonesia.
- 929 Nature Geoscience, 14, 484-490. 10.1038/s41561-021-00785-2
- 930 Dorrepaal, E., Toet, S., van Logtestijn, R.S.P., Swart, E., van de Weg, M.J., Callaghan, T.V., Aerts, R., 2009.
- Carbon respiration from subsurface peat accelerated by climate warming in the subarctic. Nature, 460,
- 932 616-619. https://doi.org/10.1038/nature08216
- 933 Dunn, O.J., 1964. Multiple Comparisons Using Rank Sums. Technometrics, 6, 241-252. 10.2307/1266041
- 934 Evans, C.D., Peacock, M., Baird, A.J., Artz, R.R.E., Burden, A., Callaghan, N., Chapman, P.J., Cooper, H.M.,
- 935 Coyle, M., Craig, E., Cumming, A., Dixon, S., Gauci, V., Grayson, R.P., Helfter, C., Heppell, C.M., Holden,
- 936 J., Jones, D.L., Kaduk, J., Levy, P., Matthews, R., McNamara, N.P., Misselbrook, T., Oakley, S., Page, S.E.,
- 937 Rayment, M., Ridley, L.M., Stanley, K.M., Williamson, J.L., Worrall, F., Morrison, R., 2021. Overriding
- 938 water table control on managed peatland greenhouse gas emissions. Nature, 593, 548-552.
- 939 10.1038/s41586-021-03523-1
- 940 Fang, C., Moncrieff, J.B., 2001. The dependence of soil CO2 efflux on temperature. Soil Biology and
- 941 Biochemistry, 33, 155-165. https://doi.org/10.1016/S0038-0717(00)00125-5
- 942 Farmer, J., Matthews, R., Smith, J.U., Smith, P., Singh, B.K., 2011. Assessing existing peatland models for
- their applicability for modelling greenhouse gas emissions from tropical peat soils. Current Opinion in
- 944 Environmental Sustainability, 3, 339-349. https://doi.org/10.1016/j.cosust.2011.08.010
- 945 Fernandez-Bou, A.S., Dierick, D., Allen, M.F., Harmon, T.C., 2020. Precipitation-drainage cycles lead to hot
- moments in soil carbon dioxide dynamics in a Neotropical wet forest. Global Change Biology, 26, 5303-
- 947 5319. 10.1111/gcb.15194
- 948 Fox, J., Monette, G., 1992. Generalized Collinearity Diagnostics. Journal of the American Statistical
- 949 Association, 87, 178-183. https://doi.org/10.2307/2290467
- 950 Frankard, P., Ghiette, P., Hindryckx, M.-N., Schumacker, R., Wastiaux, C., 1998. Peatlands of Wallony (S-
- 951 Belgium), SUO, Helsinki, Finland, pp. 33-37.
- 952 Frei, S., Knorr, K.H., Peiffer, S., Fleckenstein, J.H., 2012. Surface micro-topography causes hot spots of
- 953 biogeochemical activity in wetland systems: A virtual modeling experiment. Journal of Geophysical
- 954 Research: Biogeosciences, 117. https://doi.org/10.1029/2012JG002012
- García-García, A., Cuesta-Valero, F.J., Miralles, D.G., Mahecha, M.D., Quaas, J., Reichstein, M., Zscheischler,
- J., Peng, J., 2023. Soil heat extremes can outpace air temperature extremes. Nature Climate Change, 13,
- 957 1237-1241. 10.1038/s41558-023-01812-3
- 958 Goemaere, E., Demarque, S., Dreesen, R., Declercq, P.-Y.J.G., 2016. The geological and cultural heritage of
- the Caledonian Stavelot-Venn Massif, Belgium. 8, 211-233
- 960 Gupta, H.V., Kling, H., Yilmaz, K.K., Martinez, G.F., 2009. Decomposition of the mean squared error and
- 961 NSE performance criteria: Implications for improving hydrological modelling. Journal of Hydrology, 377,
- 962 80-91. https://doi.org/10.1016/j.jhydrol.2009.08.003
- Hair, J., Black, W., Babin, B., Anderson, R., 2010. Multivariate Data Analysis: A Global Perspective.
- 964 Harris, A., Baird, A.J., 2019. Microtopographic Drivers of Vegetation Patterning in Blanket Peatlands

- 965 Recovering from Erosion. Ecosystems, 22, 1035-1054. https://doi.org/10.1007/s10021-018-0321-6
- 966 Hatala, J.A., Detto, M., Sonnentag, O., Deverel, S.J., Verfaillie, J., Baldocchi, D.D., 2012. Greenhouse gas
- 967 (CO2, CH4, H2O) fluxes from drained and flooded agricultural peatlands in the Sacramento-San Joaquin
- 968 Delta. Agriculture, Ecosystems & Environment, 150, 1-18. https://doi.org/10.1016/j.agee.2012.01.009
- 969 Henrion, M., Li, Y., Koganti, T., Bechtold, M., Jonard, F., Opfergelt, S., Vanacker, V., Van Oost, K., Lambot,
- 970 S., 2024. Mapping and monitoring peatlands in the Belgian Hautes Fagnes: Insights from Ground-
- 971 penetrating radar and Electromagnetic induction characterization. Geoderma Regional, 37.
- 972 10.1016/j.geodrs.2024.e00795
- 973 Henrion, M., Li, Y., Wu, K., Jonard, F., Opfergelt, S., Vanacker, V., Van Oost, K., Lambot, S., 2025. Drone-
- 974 Borne Ground-Penetrating Radar Reveals Spatiotemporal Moisture Dynamics in Peatland Root Zones.
- 975 Available at SSRN. 10.2139/ssrn.5098978
- 976 Hopple, A.M., Wilson, R.M., Kolton, M., Zalman, C.A., Chanton, J.P., Kostka, J., Hanson, P.J., Keller, J.K.,
- 977 Bridgham, S.D., 2020. Massive peatland carbon banks vulnerable to rising temperatures. Nature
- 978 Communications, 11, 2373. 10.1038/s41467-020-16311-8
- 979 Hoyos-Santillan, J., Lomax, B.H., Large, D., Turner, B.L., Boom, A., Lopez, O.R., Sjögersten, S., 2016. Quality
- 980 not quantity: Organic matter composition controls of CO2 and CH4 fluxes in neotropical peat profiles.
- 981 Soil Biology and Biochemistry, 103, 86-96. https://doi.org/10.1016/j.soilbio.2016.08.017
- 982 Hoyt, A.M., Gandois, L., Eri, J., Kai, F.M., Harvey, C.F., Cobb, A.R., 2019. CO2 emissions from an undrained
- tropical peatland: Interacting influences of temperature, shading and water table depth. Global Change
- 984 Biology, 25, 2885-2899. https://doi.org/10.1111/gcb.14702
- 985 Huang, N., Gu, L., Black, T.A., Wang, L., Niu, Z., 2015. Remote sensing-based estimation of annual soil
- 986 respiration at two contrasting forest sites. Journal of Geophysical Research: Biogeosciences, 120, 2306-
- 987 2325. https://doi.org/10.1002/2015JG003060
- 988 Huang, Y., Ciais, P., Luo, Y., Zhu, D., Wang, Y., Qiu, C., Goll, D.S., Guenet, B., Makowski, D., De Graaf, I.,
- 989 Leifeld, J., Kwon, M.J., Hu, J., Qu, L., 2021. Tradeoff of CO2 and CH4 emissions from global peatlands
- 990 under water-table drawdown. Nature Climate Change, 11, 618-622. https://doi.org/10.1038/s41558-
- 991 021-01059-w
- 992 Ishikura, K., Darung, U., Inoue, T., Hatano, R., 2018. Variation in Soil Properties Regulate Greenhouse Gas
- 993 Fluxes and Global Warming Potential in Three Land Use Types on Tropical Peat, Atmosphere.
- 994 Jovani-Sancho, A.J., Cummins, T., Byrne, K.A., 2021. Soil carbon balance of afforested peatlands in the
- 995 maritime temperate climatic zone. Global Change Biology, 27, 3681-3698.
- 996 https://doi.org/10.1111/gcb.15654
- 997 Junttila, S., Kelly, J., Kljun, N., Aurela, M., Klemedtsson, L., Lohila, A., Nilsson, M.B., Rinne, J., Tuittila, E.-S.,
- 998 Vestin, P., Weslien, P., Eklundh, L., 2021. Upscaling Northern Peatland CO2 Fluxes Using Satellite Remote
- 999 Sensing Data, Remote Sensing.
- 1000 Juszczak, R., Humphreys, E., Acosta, M., Michalak-Galczewska, M., Kayzer, D., Olejnik, J., 2013. Ecosystem
- respiration in a heterogeneous temperate peatland and its sensitivity to peat temperature and water
- table depth. Plant and Soil, 366, 505-520. 10.1007/s11104-012-1441-y
- 1003 Kannenberg, S.A., Bowling, D.R., Anderegg, W.R.L., 2020. Hot moments in ecosystem fluxes: High GPP
- anomalies exert outsized influence on the carbon cycle and are differentially driven by moisture
- availability across biomes. Environmental Research Letters, 15, 054004. 10.1088/1748-9326/ab7b97
- 1006 Kechavarzi, C., Dawson, Q., Bartlett, M., Leeds-Harrison, P.B., 2010. The role of soil moisture, temperature
- and nutrient amendment on CO2 efflux from agricultural peat soil microcosms. Geoderma, 154, 203-
- $1008 \qquad \hbox{210. https://doi.org/10.1016/j.geoderma.2009.02.018}$

- 1009 Kelly, J., Kljun, N., Eklundh, L., Klemedtsson, L., Liljebladh, B., Olsson, P.-O., Weslien, P., Xie, X., 2021.
- 1010 Modelling and upscaling ecosystem respiration using thermal cameras and UAVs: Application to a
- 1011 peatland during and after a hot drought. Agricultural and Forest Meteorology, 300, 108330.
- 1012 https://doi.org/10.1016/j.agrformet.2021.108330
- 1013 Kim, J., Verma, S.B., 1992. Soil surface CO2 flux in a Minnesota peatland. Biogeochemistry, 18, 37-51.
- 1014 10.1007/BF00000425
- 1015 Knox, S.H., Sturtevant, C., Matthes, J.H., Koteen, L., Verfaillie, J., Baldocchi, D., 2015. Agricultural peatland
- 1016 restoration: effects of land-use change on greenhouse gas (CO2 and CH4) fluxes in the Sacramento-San
- 1017 Joaquin Delta. Global Change Biology, 21, 750-765. https://doi.org/10.1111/gcb.12745
- 1018 Krichels, A.H., Yang, W.H., 2019. Dynamic Controls on Field-Scale Soil Nitrous Oxide Hot Spots and Hot
- 1019 Moments Across a Microtopographic Gradient. Journal of Geophysical Research: Biogeosciences, 124,
- 1020 3618-3634. https://doi.org/10.1029/2019JG005224
- 1021 Kuzyakov, Y., Blagodatskaya, E., 2015. Microbial hotspots and hot moments in soil: Concept & review. Soil
- 1022 Biology and Biochemistry, 83, 184-199. https://doi.org/10.1016/j.soilbio.2015.01.025
- 1023 Lai, D.Y.F., Roulet, N.T., Humphreys, E.R., Moore, T.R., Dalva, M., 2012. The effect of atmospheric
- 1024 turbulence and chamber deployment period on autochamber CO₂ and CH₄
- flux measurements in an ombrotrophic peatland. Biogeosciences, 9, 3305-3322. 10.5194/bg-9-3305-
- 1026 2012
- 1027 Lai, J., Zhu, W., Cui, D., Mao, L., 2023. Extension of the glmm.hp package to zero-inflated generalized linear
- mixed models and multiple regression. Journal of Plant Ecology, 16. 10.1093/jpe/rtad038
- 1029 Lai, J., Zou, Y., Zhang, S., Zhang, X., Mao, L., 2022. glmm.hp: an R package for computing individual effect
- 1030 of predictors in generalized linear mixed models. Journal of Plant Ecology, 15, 1302-1307.
- 1031 10.1093/jpe/rtac096 %J Journal of Plant Ecology
- 1032 Lees, K.J., Quaife, T., Artz, R.R.E., Khomik, M., Clark, J.M., 2018. Potential for using remote sensing to
- 1033 estimate carbon fluxes across northern peatlands A review. Science of The Total Environment, 615,
- 1034 857-874. https://doi.org/10.1016/j.scitotenv.2017.09.103
- 1035 Leifeld, J., Klein, K., Wüst-Galley, C., 2020. Soil organic matter stoichiometry as indicator for peatland
- 1036 degradation. Scientific Reports, 10, 7634. 10.1038/s41598-020-64275-y
- 1037 Leifeld, J., Menichetti, L., 2018. The underappreciated potential of peatlands in global climate change
- 1038 mitigation strategies. Nature Communications, 9, 1071. 10.1038/s41467-018-03406-6
- Leifeld, J., Steffens, M., Galego-Sala, A., 2012. Sensitivity of peatland carbon loss to organic matter quality.
- Geophysical Research Letters, 39. https://doi.org/10.1029/2012GL051856
- 1041 Leifeld, J., Wüst-Galley, C., Page, S., 2019. Intact and managed peatland soils as a source and sink of GHGs
- 1042 from 1850 to 2100. Nature Climate Change, 9, 945-947. 10.1038/s41558-019-0615-5
- 1043 Leon, E., Vargas, R., Bullock, S., Lopez, E., Panosso, A.R., La Scala, N., 2014. Hot spots, hot moments, and
- spatio-temporal controls on soil CO2 efflux in a water-limited ecosystem. Soil Biology and Biochemistry,
- 1045 77, 12-21. https://doi.org/10.1016/j.soilbio.2014.05.029
- 1046 Li, Y., Henrion, M., Moore, A., Lambot, S., Opfergelt, S., Vanacker, V., Jonard, F., Van Oost, K., 2024. Factors
- controlling peat soil thickness and carbon storage in temperate peatlands based on UAV high-resolution
- 1048 remote sensing. Geoderma, 449, 117009. https://doi.org/10.1016/j.geoderma.2024.117009
- 1049 Li, Z.-L., Wu, H., Wang, N., Qiu, S., Sobrino, J.A., Wan, Z., Tang, B.-H., Yan, G., 2013. Land surface emissivity
- 1050 retrieval from satellite data. International Journal of Remote Sensing, 34, 3084-3127.
- 1051 10.1080/01431161.2012.716540
- 1052 Marwanto, S., Agus, F., 2014. Is CO2 flux from oil palm plantations on peatland controlled by soil moisture

- and/or soil and air temperatures? Mitigation and Adaptation Strategies for Global Change, 19, 809-819.
- 1054 10.1007/s11027-013-9518-3
- 1055 Mason, C.W., Stoof, C.R., Richards, B.K., Das, S., Goodale, C.L., Steenhuis, T.S., 2017. Hotspots of Nitrous
- 1056 Oxide Emission in Fertilized and Unfertilized Perennial Grasses. Soil Science Society of America Journal,
- 1057 81, 450-458. https://doi.org/10.2136/sssaj2016.08.0249
- 1058 McClain, M.E., Boyer, E.W., Dent, C.L., Gergel, S.E., Grimm, N.B., Groffman, P.M., Hart, S.C., Harvey, J.W.,
- Johnston, C.A., Mayorga, E., McDowell, W.H., Pinay, G., 2003. Biogeochemical Hot Spots and Hot
- 1060 Moments at the Interface of Terrestrial and Aquatic Ecosystems. Ecosystems, 6, 301-312.
- 1061 10.1007/s10021-003-0161-9
- 1062 McNamara, N.P., Plant, T., Oakley, S., Ward, S., Wood, C., Ostle, N., 2008. Gully hotspot contribution to
- landscape methane (CH4) and carbon dioxide (CO2) fluxes in a northern peatland. Science of The Total
- 1064 Environment, 404, 354-360. https://doi.org/10.1016/j.scitotenv.2008.03.015
- 1065 Meehl, G.A., Tebaldi, C., 2004. More Intense, More Frequent, and Longer Lasting Heat Waves in the 21st
- 1066 Century. Science, 305, 994-997. 10.1126/science.1098704
- 1067 Minasny, B., Berglund, Ö., Connolly, J., Hedley, C., de Vries, F., Gimona, A., Kempen, B., Kidd, D., Lilja, H.,
- 1068 Malone, B., McBratney, A., Roudier, P., O'Rourke, S., Rudiyanto, Padarian, J., Poggio, L., ten Caten, A.,
- 1069 Thompson, D., Tuve, C., Widyatmanti, W., 2019. Digital mapping of peatlands A critical review. Earth-
- 1070 Science Reviews, 196, 102870. https://doi.org/10.1016/j.earscirev.2019.05.014
- 1071 Moore, H.E., Comas, X., Briggs, M.A., Reeve, A.S., Slater, L.D., 2024. Indications of preferential
- groundwater seepage feeding northern peatland pools. Journal of Hydrology, 638, 131479.
- 1073 https://doi.org/10.1016/j.jhydrol.2024.131479
- 1074 Moore, P.A., Lukenbach, M.C., Thompson, D.K., Kettridge, N., Granath, G., Waddington, J.M., 2019.
- Assessing the peatland hummock–hollow classification framework using high-resolution elevation
- models: implications for appropriate complexity ecosystem modeling. Biogeosciences, 16, 3491-3506.
- 1077 10.5194/bg-16-3491-2019
- 1078 Mormal, P., Tricot, C., 2004. Aperçu climatique des Hautes-Fagnes, Institut Royal météorologique de
- 1079 Belgique, Brussel.
- 1080 Murdoch, D.J., Chow, E.D., 1996. A Graphical Display of Large Correlation Matrices. The American
- 1081 Statistician, 50, 178-180. https://doi.org/10.2307/2684435
- 1082 Nakagawa, S., Johnson, P.C.D., Schielzeth, H., 2017. The coefficient of determination R2 and intra-class
- correlation coefficient from generalized linear mixed-effects models revisited and expanded. Journal of
- 1084 The Royal Society Interface, 14, 20170213. 10.1098/rsif.2017.0213
- 1085 Nichols, D.S., 1998. Temperature of upland and peatland soils in a north central Minnesota forest.
- 1086 Canadian Journal of Soil Science, 78, 493-509. 10.4141/S96-030
- Pajula, R., Purre, A.-H., 2021. NDVI as a proxy to estimate the CO2 fluxes in peatlands: example of alkaline
- fen, The 16th International Peatland Congress: Peatland and Peat Source of Ecosystem Services, Tallinn,
- 1089 Estonia
- 1090 Pinheiro, J.C., Bates, D.M., 2000. Fitting Linear Mixed-Effects Models. in: Pinheiro, J.C., Bates, D.M. (Eds.),
- 1091 Mixed-Effects Models in S and S-PLUS. Springer New York, New York, NY, pp. 133-199.
- 1092 Prananto, J.A., Minasny, B., Comeau, L.-P., Rudiyanto, R., Grace, P., 2020. Drainage increases CO2 and N2O
- 1093 emissions from tropical peat soils. Global Change Biology, 26, 4583-4600.
- 1094 https://doi.org/10.1111/gcb.15147
- Rey-Sanchez, C., Arias-Ortiz, A., Kasak, K., Chu, H., Szutu, D., Verfaillie, J., Baldocchi, D., 2022. Detecting
- Hot Spots of Methane Flux Using Footprint-Weighted Flux Maps. J Geophys Res Biogeosci, 127,

- 1097 e2022JG006977. 10.1029/2022jg006977
- 1098 Rhoswen, L., Rhoswen, L., Nicholas, K., Nicholas, K., Devito, K.J., Kevin, J.D., Kevin, D., Richard, M.P.,
- 1099 Richard, M.P., Carl, M., Carl, A.M., Waddington, J.M., James, M.W., Stefan, K., Stefan, K., 2018.
- 1100 Disturbance Impacts on Thermal Hot Spots and Hot Moments at the Peatland-Atmosphere Interface.
- 1101 Geophysical Research Letters. 10.1002/2017gl075974
- 1102 Risk, D., Nickerson, N., Creelman, C., McArthur, G., Owens, J., 2011. Forced Diffusion soil flux: A new
- technique for continuous monitoring of soil gas efflux. Agricultural and Forest Meteorology, 151, 1622-
- 1104 1631. https://doi.org/10.1016/j.agrformet.2011.06.020
- 1105 Rowson, J., Worrall, F., Evans, M., Dixon, S., 2012. Predicting soil respiration from peatlands. Science of
- 1106 The Total Environment, 442C, 397-404. 10.1016/j.scitotenv.2012.10.021
- 1107 Ryan, M.G., Law, B.E., 2005. Interpreting, measuring, and modeling soil respiration. Biogeochemistry, 73,
- 1108 3-27. 10.1007/s10533-004-5167-7
- 1109 Schubert, P., Eklundh, L., Lund, M., Nilsson, M., 2010. Estimating northern peatland CO2 exchange from
- 1110 MODIS time series data. Remote Sensing of Environment, 114, 1178-1189
- 1111 https://doi.org/10.1016/j.rse.2010.01.005
- 1112 Shrout, P.E., Fleiss, J.L., 1979. Intraclass correlations: Uses in assessing rater reliability. Psychological
- 1113 Bulletin, 86, 420-428. 10.1037/0033-2909.86.2.420
- 1114 Simpson, G., 2023. Drivers of peatland CO₂ balance: a fusion of UAV remote sensing and
- micrometeorology. Doctoral dissertation Thesis, The University of Edinburgh, U.K., 57-157 pp.
- 1116 Snyder, W.C., Wan, Z., Zhang, Y., Feng, Y.Z., 1998. Classification-based emissivity for land surface
- temperature measurement from space. International Journal of Remote Sensing, 19, 2753-2774.
- 1118 10.1080/014311698214497
- 1119 Sougnez, N., Vanacker, V., 2011. The topographic signature of Quaternary tectonic uplift in the Ardennes
- massif (Western Europe). Hydrol. Earth Syst. Sci., 15, 1095-1107. https://doi.org/10.5194/hess-15-
- 1121 1095-2011
- 1122 Steenvoorden, J., Bartholomeus, H., Limpens, J., 2023. Less is more: Optimizing vegetation mapping in
- peatlands using unmanned aerial vehicles (UAVs). International Journal of Applied Earth Observation
- and Geoinformation, 117, 103220. https://doi.org/10.1016/j.jag.2023.103220
- 1125 Stoy, P.C., Street, L.E., Johnson, A.V., Prieto-Blanco, A., Ewing, S.A., 2012. Temperature, Heat Flux, and
- 1126 Reflectance of Common Subarctic Mosses and Lichens under Field Conditions: Might Changes to
- 1127 Community Composition Impact Climate-Relevant Surface Fluxes? Arctic, Antarctic, and Alpine Research,
- 1128 44, 500-508. 10.1657/1938-4246-44.4.500
- 1129 Swails, E.E., Ardón, M., Krauss, K.W., Peralta, A.L., Emanuel, R.E., Helton, A.M., Morse, J.L., Gutenberg, L.,
- 1130 Cormier, N., Shoch, D., Settlemyer, S., Soderholm, E., Boutin, B.P., Peoples, C., Ward, S., 2022. Response
- of soil respiration to changes in soil temperature and water table level in drained and restored peatlands
- of the southeastern United States. Carbon Balance and Management, 17, 18. 10.1186/s13021-022-
- 1133 00219-5
- 1134 Tokida, T., Miyazaki, T., Mizoguchi, M., 2005. Ebullition of methane from peat with falling atmospheric
- pressure. Geophysical Research Letters, 32. https://doi.org/10.1029/2005GL022949
- 1136 Tokida, T., Miyazaki, T., Mizoguchi, M., Nagata, O., Takakai, F., Kagemoto, A., Hatano, R., 2007. Falling
- atmospheric pressure as a trigger for methane ebullition from peatland. Global Biogeochemical Cycles,
- 1138 21. https://doi.org/10.1029/2006GB002790
- 1139 Treat, C.C., Wollheim, W.M., Varner, R.K., Grandy, A.S., Talbot, J., Frolking, S., 2014. Temperature and peat
- 1140 type control CO2 and CH4 production in Alaskan permafrost peats. Global Change Biology, 20, 2674-

- 1141 2686. 10.1111/gcb.12572
- 1142 Turetsky, M.R., Benscoter, B., Page, S., Rein, G., van der Werf, G.R., Watts, A., 2015. Global vulnerability of
- peatlands to fire and carbon loss. Nature Geoscience, 8, 11-14. 10.1038/ngeo2325
- 1144 UNEP, 2022. Global Peatlands Assessment The State of the World's Peatlands: Evidence for action
- toward the conservation, restoration, and sustainable management of peatlands. 9789280739916,
- 1146 Global Peatlands Initiative, United Nations Environment Programme.
- van Giersbergen, Q., Barthelmes, A., Couwenberg, j., Fritz, C., Lång, K., Martin, N., Tanneberger, F., 2024.
- 1148 Identifying hotspots of greenhouse gas emissions from drained peatlands in the European Union.
- 1149 PREPRINT (Version 1) available at Research Square. https://doi.org/10.21203/rs.3.rs-4629642/v1
- 1150 Walcker, R., Le Lay, C., Gandois, L., Elger, A., Jassey, V.E.J., 2025. High-resolution mapping of peatland CO2
- 1151 fluxes using drone multispectral images. Ecological Informatics, 103060
- 1152 https://doi.org/10.1016/j.ecoinf.2025.103060
- 1153 Walker, T.N., Garnett, M.H., Ward, S.E., Oakley, S., Bardgett, R.D., Ostle, N.J., 2016. Vascular plants
- 1154 promote ancient peatland carbon loss with climate warming. Global Change Biology, 22, 1880-1889.
- 1155 https://doi.org/10.1111/gcb.13213
- 1156 Wang, H., Richardson, C.J., Ho, M., 2015a. Dual controls on carbon loss during drought in peatlands.
- 1157 Nature Climate Change, 5, 584-587. 10.1038/NCLIMATE2643
- 1158 Wang, H., Tian, J., Chen, H., Ho, M., Vilgalys, R., Bu, Z.-J., Liu, X., Richardson, C.J., 2021. Vegetation and
- microbes interact to preserve carbon in many wooded peatlands. Communications Earth & Environment,
- 1160 2, 67. 10.1038/s43247-021-00136-4
- 1161 Wang, M., Moore, T.R., Talbot, J., Riley, J.L., 2015b. The stoichiometry of carbon and nutrients in peat
- 1162 formation. Global Biogeochemical Cycles, 29, 113-121. https://doi.org/10.1002/2014GB005000
- 1163 Wangari, E.G., Mwanake, R.M., Kraus, D., Werner, C., Gettel, G.M., Kiese, R., Breuer, L., Butterbach-Bahl,
- 1164 K., Houska, T., 2022. Number of Chamber Measurement Locations for Accurate Quantification of
- Landscape-Scale Greenhouse Gas Fluxes: Importance of Land Use, Seasonality, and Greenhouse Gas
- 1166 Type. Journal of Geophysical Research: Biogeosciences, 127, e2022JG006901.
- 1167 https://doi.org/10.1029/2022JG006901
- 1168 Wangari, E.G., Mwangada Mwanake, R., Houska, T., Kraus, D., Gettel, G.M., Kiese, R., Breuer, L.,
- 1169 Butterbach-Bahl, K., 2023. Identifying landscape hot and cold spots of soil greenhouse gas fluxes by
- 1170 combining field measurements and remote sensing data. Biogeosciences, 20, 5029-5067. 10.5194/bg-
- 1171 20-5029-2023
- 1172 Webster, K.L., Creed, I.F., Beall, F.D., Bourbonnière, R.A., 2008. Sensitivity of catchment-aggregated
- 1173 estimates of soil carbon dioxide efflux to topography under different climatic conditions. Journal of
- 1174 Geophysical Research: Biogeosciences, 113. https://doi.org/10.1029/2008JG000707
- 1175 Widyastuti, M.T., Minasny, B., Padarian, J., Maggi, F., Aitkenhead, M., Beucher, A., Connolly, J., Fiantis, D.,
- Kidd, D., Ma, Y., Macfarlane, F., Robb, C., Rudiyanto, Setiawan, B.I., Taufik, M., 2025. Digital mapping of
- 1177 peat thickness and carbon stock of global peatlands. CATENA, 258, 109243
- 1178 https://doi.org/10.1016/j.catena.2025.109243
- 1179 Wilkinson, S.L., Andersen, R., Moore, P.A., Davidson, S.J., Granath, G., Waddington, J.M., 2023. Wildfire
- 1180 and degradation accelerate northern peatland carbon release. Nature Climate Change, 13, 456-461.
- 1181 https://doi.org/10.1038/s41558-023-01657-w
- 1182 Wilson, D., Dixon, S.D., Artz, R.R.E., Smith, T.E.L., Evans, C.D., Owen, H.J.F., Archer, E., Renou-Wilson, F.,
- 2015. Derivation of greenhouse gas emission factors for peatlands managed for extraction in the
- Republic of Ireland and the United Kingdom. Biogeosciences, 12, 5291-5308. 10.5194/bg-12-5291-2015

- 1185 Wood, T.E., Detto, M., Silver, W.L., 2013. Sensitivity of Soil Respiration to Variability in Soil Moisture and
- 1186 Temperature in a Humid Tropical Forest. PLOS ONE, 8, e80965. 10.1371/journal.pone.0080965
- 1187 Wright, E.L., Black, C.R., Turner, B.L., Sjögersten, S., 2013. Environmental controls of temporal and spatial
- 1188 variability in and fluxes in a neotropical peatland. Global Change Biology, 19, 3775-3789.
- 1189 https://doi.org/10.1111/gcb.12330
- 1190 Wutzler, T., Perez-Priego, O., Morris, K., El-Madany, T.S., Migliavacca, M., 2020. Soil CO2 efflux errors are
- lognormally distributed implications and guidance. Geosci. Instrum. Method. Data Syst., 9, 239-254.
- 1192 10.5194/gi-9-239-2020
- 1193 Xu, J., Morris, P.J., Liu, J., Holden, J., 2018. PEATMAP: Refining estimates of global peatland distribution
- 1194 based on a meta-analysis. CATENA, 160, 134-140. https://doi.org/10.1016/j.catena.2017.09.010
- 1195 Yu, Z., Loisel, J., Brosseau, D.P., Beilman, D.W., Hunt, S.J., 2010. Global peatland dynamics since the Last
- 1196 Glacial Maximum. Geophysical Research Letters, 37. https://doi.org/10.1029/2010GL043584
- 1197 Zhang, C., Comas, X., Brodylo, D., 2020. A Remote Sensing Technique to Upscale Methane Emission Flux
- in a Subtropical Peatland. Journal of Geophysical Research: Biogeosciences, 125, e2020JG006002.
- 1199 https://doi.org/10.1029/2020JG006002
- 1200 Zou, J., Ziegler, A.D., Chen, D., McNicol, G., Ciais, P., Jiang, X., Zheng, C., Wu, J., Wu, J., Lin, Z., He, X., Brown,
- 1201 L.E., Holden, J., Zhang, Z., Ramchunder, S.J., Chen, A., Zeng, Z., 2022. Rewetting global wetlands
- 1202 effectively reduces major greenhouse gas emissions. Nature Geoscience, 15, 627-632. 10.1038/s41561-
- 1203 022-00989-0

1204